Clays and Clay Minerals, Vol. 68, No. 2:115–134, 2020

THE FORMATION OF CLAY MINERALS IN THE MUDFLATS OF BOLIVIAN SALARS

Jennifer L. Bentz* and Ronald C. Peterson

[1]Department of Geological Sciences and Geological Engineering, Queen's University, 36 Union Street, Kingston, ON K7L 3N6, Canada

Abstract—Understanding clay-mineral assemblages forming in saline lakes aids in reconstructing paleoenvironments on Earth and other terrestrial planets; this is because authigenic phyllosilicates are sensitive to the prevailing geochemical conditions present during formation. In most geochemical models, evaporative concentration favors sepiolite with increasing silica and Mg^{2+} concentrations without considering the role of the biogenic removal of silica from solution by diatoms. In the present study, phyllosilicates occurring in the mudflats of Bolivian salars were investigated to aid in understanding the geochemical factors that control mineral assemblages forming in (SO_4^{2-})- and (Cl^-)-rich environments in relation to dissolved silica. From transects across the mudflats, the physical, chemical, and mineralogical characteristics of the bulk sediment and the <2 μm fraction of each sedimentary layer were analyzed. From these analyses, three types of sediments were identified: (1) regolith sediments dominated by Al-dioctahedral smectite, illite, and chlorite; (2) detritus-rich mudflat sediments with Mg-trioctahedral smectite and Al-dioctahedral smectite along with illite and chlorite; and (3) authigenic mudflat sediments dominated by poorly formed Mg-trioctahedral smectite, kerolite, and biogenic silica. The absence of sepiolite-palygorskite in the salars is the result of excessively high Mg:Si ratios within the waters. In the surface water Mg becomes enriched relative to Si as diatoms remove dissolved Si from solution through biologically mediated uptake. The geochemical conditions present within the salars that act to preserve the diatom frustules and prevent their dissolution include: neutral–slightly alkaline pH solutions, cold temperatures, shallow water, and high salinity. Under these conditions the formation of sepiolite is restricted by the small amount of dissolved silica, despite the silica-rich environment. The formation of Mg-smectite and kerolite is favored under these conditions.

Keywords—Authigenic · Bolivian Altiplano · Clay · Diatom frustule · Kerolite · Magnesium · Salar · Saponite · Stevensite · Sulfate-rich brine

INTRODUCTION

Authigenic phyllosilicates commonly form in continental aqueous sedimentary environments characterized by alkaline-saline conditions developed under arid climates either by neoformation or transformation (Meunier 2005; Bristow and Milliken 2011; Deocampo 2015). Concentration of these lake waters by evaporation leads to a complex series of precipitation reactions as the brines evolve and control the mineral assemblages that are present. Phyllosilicates forming from direct precipitation in alkaline lakes tend to be Mg-rich minerals such as sepiolite, stevensite, kerolite, saponite, and hectorite (Jones 1986; Meunier 2005). The major geochemical factors controlling the phyllosilicate minerals that precipitate may include: pH, alkalinity, element ratios, the presence or absence of detrital material, dissolved CO_2 from biological activity, salinity, and the activities of Mg^{2+}, Si^{4+}, Al^{3+}, Ca^{2+}, and Fe^{3+} in solution (Jones and Galán 1988; Weaver 1989; Deocampo 2005; Bristow and Milliken 2011). The evolutionary pathway followed by brines evaporating in closed-basin lakes depends on the concentrations of HCO_3^- and Ca^{2+} during calcite precipitation (Hardie and Eugster 1970). During this critical first step, solutions evolve during calcite precipitation towards bicarbonate-rich brines if $[HCO_3^-] > [Ca^{2+}]$ and towards sulfate- and/or chloride-rich brines if $[HCO_3^-] < [Ca^{2+}]$ (Hardie and Eugster 1970).

The authigenic phyllosilicates formed in waters that evolve toward bicarbonate-rich brines have been studied extensively in Lake Chad, Africa (Gac et al. 1977); Lake Yao, Africa (Darragi and Tardy 1987); Abert Lake, Oregon, USA (Jones and Weir 1983; Banfield et al. 1991); Searles Lake, California, USA (Hay et al. 1991); Jurassic Lake T'oo'dichi, Colorado, USA (Turner and Fishman 1991); the Pleistocene Amboseli basin, Kenya (Stoessell and Hay 1978); the Miocene Vallecas-Vicálvaro and Cabañas-Yunclillos deposits, Spain (Galán and Castillo 1984); and the Miocene Eskişehir basin, Turkey (Ece and Çoban 1994; Kadir et al. 2016). Jones and Galán (1988) summarized these bicarbonate-rich systems with regard to silicate minerals outlining the conditions that favor the formation of certain Mg-rich clays over others during evaporative concentration. Brackish waters with a neutral to slightly alkaline pH and high Si activity favor the precipitation of palygorskite in detritus-rich environments. Examples include alluvial-lacustrine margins and sepiolite where reactive detritus is limited and Al is immobilized, such as in calcareous soils and near springs (Jones and Galán 1988; Birsoy 2002; Bristow and Milliken 2011). With increasing pH, decreasing activity of silica, and/or high concentrations of Mg^{2+} in solution, trioctahedral smectites form where the mineralogy is determined by the amount of detrital clay and geochemistry of the solutions (Badaut and Risacher 1983; Calvo et al. 1999; Larsen 2008). Lastly, in the most saline conditions near basin centers and areas with repeated wetting and drying cycles, high K^+/Mg^{2+} activity ratios and high pH result in K uptake into smectite interlayers and the formation of illite-like domains as well as the neoformation of 10 Å clays (Turner and Fishman 1991; Hay and Kyser 2001; Hover and Ashley 2003; Furquim et al. 2010).

The other half of the geochemical divide produces sulfate- and chloride-rich brines. For these systems the pH of the evaporating brines can be neutral to slightly alkaline or can be acidic. Moderately alkaline, sulfate-rich salars have been found on the

* E-mail address of corresponding author:
jennifer.bentz@queensu.ca
DOI: 10.1007/s42860-020-00065-x

Bolivian Altiplano where Mg-rich smectites occur if the pH is >8.5 (Badaut and Risacher 1983). For the sulfate-alkaline systems, many of the factors controlling authigenic clay formation are already described by the high pH, bicarbonate-rich systems. Conversely, acid-saline, sulfate-rich lakes have been analyzed in south Western Australia where authigenic kaolinite and Fe oxides are favored to precipitate (Bowen and Benison 2009; Story et al. 2010). These sulfate/chloride systems are high-priority analogs for understanding past environments on Mars as many layered deposits on the planet have been found with both phyllosilicates and sulfates such as Gale Crater, Mawth Vallis, and Columbus crater, all of which could have hosted paleocrater lakes (Farrand et al. 2009; Milliken et al. 2010; Wray et al. 2010, 2011). Unfortunately, modern terrestrial environments with sulfate- and chloride-rich waters are relatively rare and have not been studied extensively (Bristow and Milliken 2011). The deposits that have been found should, therefore, be analyzed in greater detail.

While the aforementioned generalizations can be helpful in establishing geochemical controls for clay-mineral formation, the complex environments created by evaporating brines across basins can make predicting clay mineral assemblages difficult. Many of the environmental conditions that favor magnesium clay formation overlap for sepiolite and Mg-smectite, especially for sulfate/chloride-rich systems in closed-basin lakes. For example, both sepiolite and Mg-smectite are favored at intermediate pH (8–9.5), intermediate alkali salinity, and groundwater-dominated input (Jones and Galán 1988; Galán and Pozo 2011). One of the main differences in the factors of formation between these two clays is the activity of silica and Mg in solution; where sepiolite is favored at high silica activities (Mg/Si ≤1 or $\log[a\mathrm{SiO}_{2(aq)}] > -4.5$) and Mg-smectite at low silica activities (Mg/Si ≥1 or $\log[a\mathrm{SiO}_{2(aq)}] < -4.5$) (Jones and Galán 1988; Galán and Pozo 2011; Tosca and Masterson 2014; Tosca 2015). For more complex systems, equilibrium activity diagrams for the $MgO\text{-}CaO\text{-}Al_2O_3\text{-}SiO_2\text{-}H_2O\text{-}CO_2\text{-}HCl$ system calculated by Birsoy (2002) found sepiolite to be favored when the pH is between 8.5–9.5 and $\log[a\mathrm{H}_2\mathrm{SiO}_4] > -4.75$. Therefore, understanding the controls of dissolved silica in solution can aid in explaining Mg-clay formation in these intermediate environments such as the salars on the Bolivian Altiplano.

Previous analysis of the surface waters suggests the sulfate-rich brines for several of the salars are brackish with pH values ranging from neutral to alkaline (7–10) and saturated with respect to dissolved Si — where the log $[a\mathrm{H}_4\mathrm{SiO}_4]$ is > –3.5 and well within the zone of sepiolite formation (Badaut and Risacher 1983; Servant-Vildary and Roux 1990; Risacher and Fritz 1991; Dejoux 1993). Characterization of the clay minerals present in the surface waters by Badaut and Risacher (1983), however, found a highly soluble authigenic Mg-smectite resembling stevensite replacing the diatom frustules. This authigenic Mg-smectite formed only in salars where the pH of the surface water was >8.2, regardless of salinity (Badaut and Risacher 1983). Diatom frustules have been cited as a source of silica for authigenic clay minerals and as a buffer for maintaining dissolved silica concentrations (Hay 1970; Stoessell and Hay 1978; Badaut and Risacher 1983; Banfield et al. 1991; Chahi et al. 1997; Deocampo 2005; Bristow and Milliken 2011; Huggett et al. 2016). The overall effect of the algae on water chemistry with respect to clay mineral assemblages has not been examined thoroughly, however.

The goal of the present study was to examine further the salars of the Bolivian Altiplano extending out into the mudflats to aid in understanding the processes of phyllosilicate formation in sulfate-rich environments related to dissolved silica. The study included the analysis of the mudflat sediments from six salars located in the Sur Lipez region of the Bolivian Altiplano. These salars provide a spectrum of varying water chemistry, mineralogy, pH, and amount of detritus.

GEOLOGICAL SETTING

The Bolivian Altiplano is a large intermontane basin (200,000 km^2) with an average elevation of 3,650 m bounded by the Cordillera Occidental to the west and Cordillera Oriental to the east (Risacher and Fritz 1991; Allmendinger et al. 1997). The climate is classified as arid, with a mean annual precipitation of <0.2 m y^{-1} and a mean evaporation rate of 1.5 m y^{-1} (Badaut and Risacher 1983; Argollo and Mourguiart 2000). The annual air temperature for the plateau is estimated to be between 5 and 10°C; the daily range may be up to 40°C, with extreme seasonal temperatures reaching –40°C, however in the winter and +25°C in the summer (Risacher and Fritz 1991; Cabrol et al. 2009). The salars are remnants of large paleolakes that occupied the intravolcanic basin including the Pleistocene Lake Ballivián, Paleolake Minchín (35,000 years BP), and Paleolake Tauca (15,000 years BP) (Argollo and Mourguiart 2000). The salars included in the current study occupy a number of small basins in the Sur Lipez region surrounded by stratovolcanoes, andesite lava flows, and ignimbrites (Fig. 1). The six salars analyzed in detail for the current study were selected based on overlap with previous research on the Altiplano. The salars chosen were: Laguna Canapa (CAN), Laguna Hedionda (HED), Laguna Ramaditas (RAM), Laguna Honda (HON), Laguna Chiar Khota (CHKT), and Laguna Chulluncani (CHU) (Fig. 1). Detailed descriptions of the salars can be found in Servant-Vildary and Roux (1990) and Risacher and Fritz (1991).

MATERIALS AND METHODS

Sampling

The salars were sampled in June of 2014 along transects extending from the outer boundary of the mudflat to the sediment–water interface under the surface water. For each sampling site, the sediments were excavated to the water table or ice layer (max 80 cm), with each sedimentary layer collected separately. Depending on the size, dryness, stability, and heterogeneity of sediments across the mudflat, the number of pits at each salar varied. Several dry depressions and slopes surrounding the basins were also sampled for comparison between pedogenic weathering and lacustrine processes for clay-mineral formation. Surface water samples were collected

https://doi.org/10.1007/s42860-020-00065-x Published online by Cambridge University Press

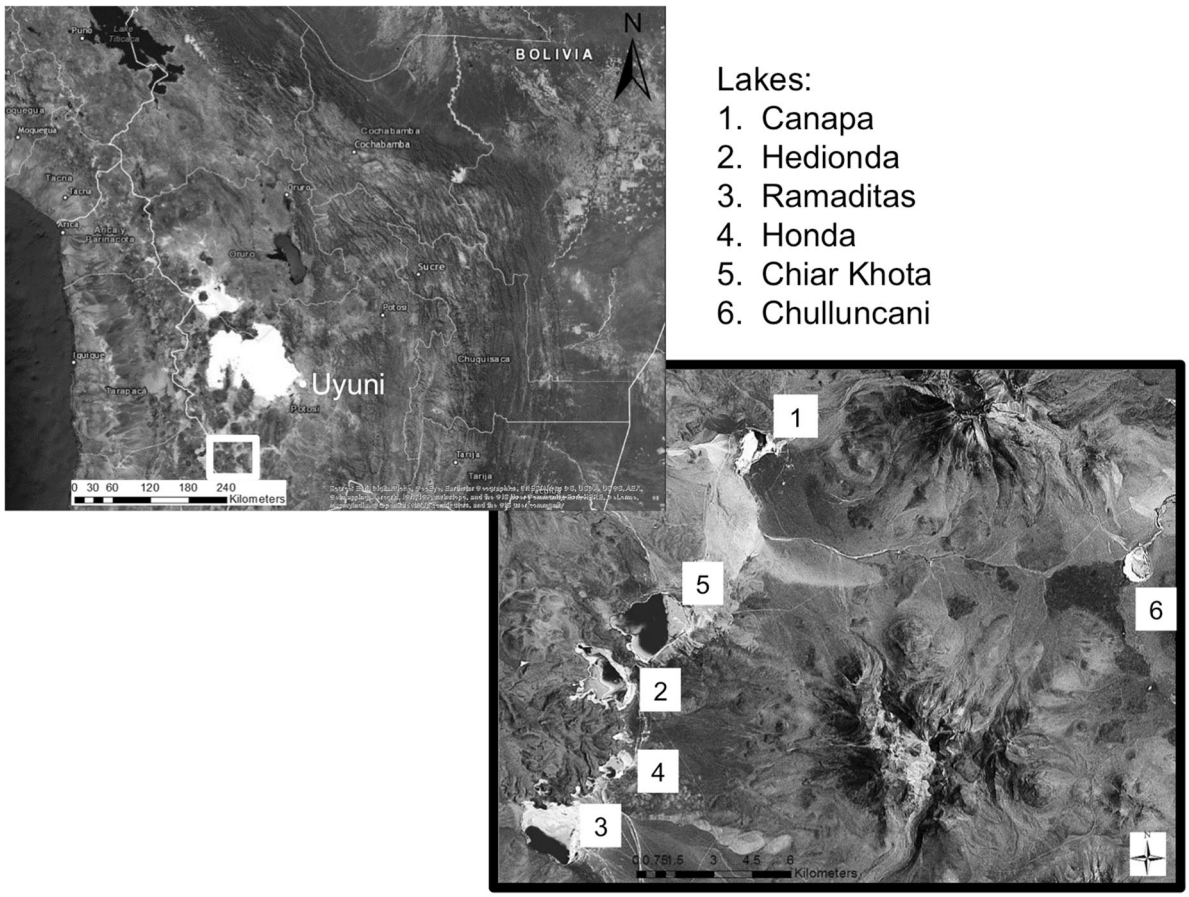

Fig. 1. Location of the study site in the Sur Lipez region of Potosi, Bolivia, and the locations of the six salars. Image of the western Sur Lipez region on a Tri-Decadal Global Landsat Orthorectified ETM+Pan Mosaic (1999–2003) acquired on January 14, 2002. Image courtesy of the US Geological Survey

for each salar. The location, pH, and salinity of the surface waters from each lake are included in Table 1. These data also include salinity and pH measurements from previous studies in 1983, 1990, 1991, and 1993. Note that the surface waters of the salars were covered with ice each morning.

X-ray Diffraction

Subsamples were air-dried and ground with a mortar and pestle to pass through a 0.125 mm sieve for bulk X-ray diffraction (XRD) analysis. Due to the soluble and fine-grained nature of the samples, the micronizing mill was not used. Corundum (Al_2O_3) was mixed with each sample (10 wt.%) as an internal standard to enable estimation of 'X-ray amorphous' phases in randomly oriented powders. For clay mineral analysis, the <2 μm fraction was separated from each sample (wet-sieved to 45 μm) by centrifugation (Moore and Reynolds 1989). Due to the low density of diatom frustules (<0.12–0.25 g cm^{-3}), separating the siliceous skeletons out of

Table 1. Location, maximum depth, and range of characteristics of each salar from 1983–current study; data from Badaut and Risacher 1983; Servant-Vildary and Roux 1990; Risacher and Fritz 1991; Dejoux 1993; Sylvestre et al. 2001

Lake	Coordinates		Salinity	Depth	pH	Classification
	S	W	g L^{-1}	cm		
CAN	21°30′17″	68°00′43”	11-52	20	7.8–9.1	Brackish–Saline
HED	21°34′19″	68°02′15″	41–72	30	6.6–8.5	Saline–Hypersaline
RAM	21°39′03″	68°04′40″	21–29	25	7.8–8.2	Brackish
HON	21°37′18″	68°03′38″	25–41	30	7.9–9.0	Brackish–Saline
CHKT	21°35′38″	68°03′28″	10–70	20	7.3–8.2	Brackish–Hypersaline
CHU	21°32′51″	67°52′51″	11–144	20	8.4–10.2	Brackish–Hypersaline

https://doi.org/10.1007/s42860-020-00065-x Published online by Cambridge University Press

the <2 μm fraction was difficult; therefore, contamination of the <2 μm fraction with frustules was assumed. Sodium hexametaphosphate was used during particle separation as a deflocculant. During the clay separation, each size fraction (>45 μm, >2 μm, and <2 μm) was weighed to determine the particle-size distribution, while the >45 μm and 45–2 μm fractions were analyzed as randomly oriented powders when required to clarify the quantitative results from the bulk analyses. The <2 μm fractions were prepared as oriented mounts via the pipette method and analyzed in their air-dried, ethylene glycol-solvated (overnight at 60°C), and heat-treated (400°C and 550°C) states. All XRD data were collected using a PANalytical X'Pert Pro diffractometer (Almelo, Netherlands) in Bragg-Brentano geometry operated at 40 kV and 45 mA using Fe-filtered CoKα radiation over the range 4–90°2θ with a 1/4° divergence slit, and 1/2° anti-scatter slit. Randomly oriented powders were prepared as back-loaded mounts and analyzed with 0.2 mm Soller slits with an effective counting time of 90 s/step; the oriented clay mounts were analyzed using 0.4 mm Soller slits with an effective counting time of 15 s/step, repeated three times to maximize intensity. For comparative analysis, 13 references clays were prepared and analyzed with the same procedures. The references were from the Source Clays Repository of The Clay Minerals Society, Iowa State University, and Pacific Northwest National Laboratory and included: K-saturated hectorite, SHCa-1 hectorite, SWa-1 ferruginous smectite, PFl-1 palygorskite, SepSp-1 sepiolite, nontronite (Washington), nontronite (Pennsylvania), saponite, bentonite (South Panther Creek), bentonite volclay, API no. 25 Upton montmorillonite, montmorillonite (Arkansas), and montmorillonite (Mississippi). All XRD data were analyzed using the Highscore Suite (Degen et al. 2014). Semi-quantitative modal mineralogy was determined via Rietveld refinement of the diffraction data collected from randomly oriented powders.

Visible and Near-Infrared Spectrometry

Near-infrared reflectance spectra were measured on the <2 μm separates relative to a USP white reference standard using an ASD TerraSpec® 4 Hi-Res Mineral Analyzer (Boulder, Colorado, USA) over the range 350–2500 nm and *RS*^{3} *Spectral Acquisition Software*. Contact reflectance spectra were collected on air-dried, ground powders at an emission angle of 0°. Reflectance data were analyzed using *The Spectral Geologist* (TSG®) developed by CSIRO Earth Science and Resource Engineering (Canberra, Australian Capital Territory, Australia).

Sediment and Water Characteristics

Sediment plugs of selected samples were mounted in epoxy and prepared as thin sections for petrographic analysis. Subsamples of each bulk fraction were treated to dissolve evaporite minerals and aid in the identification and weight of the insoluble minerals. First, gypsum was dissolved in 10% $(NH_4)_2CO_{3(aq)}$, then filtered with P4 filter paper to remove the resulting $(NH_4)_2SO_{4(aq)}$ (Eq. 1).

$$(NH_4)_2CO_{3(aq)} + CaSO_4{\cdot}2H_2O_{(s)} \leftrightarrow (NH_4)_2SO_{4(aq)} + CaCO_{3(s)} + 2H_2O_{(1)} \quad (1)$$

The filtrate was discarded and the remaining sediment and calcite sludge was then treated with 0.5 M HCl, filtered, rinsed with Milli-Q water, and dried at 60°C (Eq. 2).

$$CaCO_{3(s)} + 2HCl_{(aq)} \leftrightarrow CO_{2(g)} + CaCl_{2(aq)} + H_2O_{(1)} \quad (2)$$

Major and minor elements of surface-water samples and selected <2 μm fraction subsamples (digested in aqua regia) were analyzed for a 31 element suite using inductively coupled plasma optical emission spectroscopy, ICP-OES) (Agilent Pro-axial CCD spectrometer, Santa Clara, California, USA) by the Analytical Services Unit at Queen's University, Kingston, Ontario. The analytical accuracy was verified using the standard reference material MESS-3 for sediment samples, and the EU-H-4 standard and Cranberry-05 CRM (for Si) for the water samples. Surface water pH was measured in situ during sampling while sediment pH was measured in duplicate via the saturated paste method described by Kalro (1995) using a Vernier Tris-Compatable Flat pH Sensor and LabQuest Interface (Vernier Software and Technology, Beaverton, Oregon, USA). The morphology and qualitative chemical composition of selected <2 μm fractions were analyzed using an FEI Quanta 650 field-emission scanning electron microscope (FEG-SEM, Thermo Fisher Scientific, Hillsboro, Oregon, United States). Samples were mounted on carbon tape, carbon coated, and observed at 15 or 25 kV.

RESULTS

Three types of sediment were identified from the basins based on location, field notes, texture, and sedimentary environment: (1) regolith sediment, (2) detritus-rich mudflat sediment, and (3) mudflat sediments composed primarily of authigenic minerals. The mineralogy, texture, and abundance of surface crusts and efflorescence varied between each salar and were analyzed via XRD. The weights from the particle-size separation (data not shown) and XRD data were used to determine the mineralogy of the sediments.

X-ray Diffraction

For all the bulk sediment samples, the XRD patterns contained a broad background centered on 25°2θ (4.13 Å) representative of 'X-ray amorphous' phases such as biogenic opal (diatom frustules), volcanic glass, allophane, or imogolite (Elzea et al. 1994; Bishop et al. 2013). Major (>10%) and minor (<10%) minerals present in each sediment type for each salar are presented in Table 2. The '1-Regolith' sediments were sampled from dry depressions and margins surrounding the salars and are composed of 'X-ray amorphous' material, clay minerals, and igneous minerals consistent with the andesitic to rhyolitic surroundings (quartz, cristobalite, biotite, hornblende, albite-anorthite,

https://doi.org/10.1007/s42860-020-00065-x Published online by Cambridge University Press

clinopyroxene, and orthopyroxene) (Table 2). Sediments ranged from fine-grained (<45 μm) silt and clay in dry depressions to coarse (0.5–2 mm), poorly sorted, sub-angular grains surrounding the salar margins. The mineral suite comprising the '2-Detrital' sediments is similar to the '1-Regolith' sediment with the addition of evaporites including calcite, gypsum, halite, and sylvite (Table 2). The sediments are well sorted, sub-angular grains deposited in alluvial to deltaic environments. The '3-Authigenic' mudflat sediments are composed of 'X-ray amorphous' material, clay minerals, and a complex suite of evaporite minerals including calcite, celestine, dolomite, eugsterite, gypsum, mirabilite, authigenic quartz, authigenic cristobalite, sylvite, and ulexite (Table 2). They consist of an extremely fine-grained matrix with evaporite minerals ranging from <2 μm to 1 cm crystals of mirabilite. Surface crusts and efflorescence across the salars vary considerably; however, they are predominantly composed of Na-sulfate minerals (thenardite/mirabilite) with small quantities of analcite, aphthitalite, calcite, cristobalite, gypsum, eugsterite, halite, howlite, sylvite, and syngenite (Table 2).

X-ray Diffraction of Clay Minerals

The XRD patterns for nearly all of the oriented, <2 μm fractions displayed evidence of swelling clays and X-ray amorphous material except for sample 45, which contained X-ray amorphous phases only (Table 3).

Table 2. Generalized mineralogy of the surface evaporites, regolith, and mudflat sediments from the surrounding sediment, Laguna Canapa (CAN), Laguna Hedionda (HED), Laguna Ramaditas (RAM), Laguna Honda (HON), Laguna Chiar Khota (CHKT), and Laguna Chulluncani (CHU)

Lake	Sediment type	Major >10%*†§	Minor <10%‡
Surrounding sediment	1-Regolith	Amorphous, feldspars	Clay minerals, cristobalite, hornblende, biotite, pyroxene, quartz
Canapa	Surface	Aphthitalite, halite, thenardite	Howlite
	1-Regolith	Halite, quartz	Clay minerals, cristobalite, hornblende, biotite, pyroxene
	2-Detrital	Amorphous, *calcite*, feldspars	Calcite, clay minerals, cristobalite, halite, hornblende, biotite, pyroxene
Hedionda	Surface	Halite, thendardite,	Calcite, eugsterite, gypsum
	2-Detrital	Amorphous, *calcite,* feldspars	Calcite, cristobalite, gypsum, hornblende, biotite, pyroxene
	3-Authigenic	Amorphous, gypsum	Analcite, aphthitalite, calcite, clay minerals, eugsterite, halite, thenardite, ulexite
Ramaditas	Surface	Gypsum, calcite, halite	Calcite, cristobalite
	1-Regolith	Amorphous, Feldpars	Calcite, clay minerals, cristobalite, biotite, pyroxene
	2-Detrital	Amorphous, calcite, feldspars, pyroxene	Clay minerals, hornblende, biotite, quartz
	3-Authigenic	Amorphous, calcite, gypsum	Clay minerals, cristobalite, sylvite
Honda	Surface	Gypsum, halite, thenardite,	Amorphous, calcite, cristobalite, hörnesite
	3-Authigenic	Amorphous, gypsum, calcite	Calcite, clay minerals, cristobalite, eugsterite, gypsum, halite, quartz
Chiar Khota	Surface	Amorphous, halite	Cristobalite, dolomite, gypsum, quartz, sylvite
	3-Authigenic	Amorphous, calcite, gypsum, ulexite	As-Cu-S, calcite, celestine, clay minerals, cristobalite, dolomite, halite, hörnesite, quartz, realgar, sylvite, ulexite
Chulluncani	Surface	Amorphous, halite, thenardite	Analcite, clay minerals, cristobalite, eugsterite, gypsum, sylvite, syngenite
	2-Detrital	Amorphous, *calcite*, feldspars	Clay minerals, cristobalite, halite, hornblende, biotite, pyroxene, quartz, sylvite

* Moisture content and field descriptions identified that mirabilite is present with thenardite; italicized minerals are major constituents in specific layers. Numbers correspond to sediment type outlined in text.

† X-ray amorphous material dominated by siliceous diatom frustules identified in SEM images.

‡ For clay mineral descriptions, see Table 3.

§ Petrographic examinations of thin sections from sediment plugs for selected samples confirm the presence of biotite; feldspars range from anorthite to albite; pyroxenes include clinopyroxene and orthopyroxene.

https://doi.org/10.1007/s42860-020-00065-x Published online by Cambridge University Press

Table 3. Sediment class, pH, and clay mineral characteristics of each sample from Laguna Canapa (CAN), Laguna Hedionda (HED), Laguna Ramaditas (RAM), Laguna Honda (HON), Laguna Chiar Khota (CHKT), and Laguna Chulluncani (CHU). Clay References and Source Clays used for comparison are included

ID	Sediment Class	pH	d_{100} spacing (glycol)	(001) β_i	19–21°2θ *d* spacing (glycol)		Clay minerals
			Å	°2θ	Å	Å	
Surrounding sediment							
1	Regolith	7.4	16.7	2.6	5.70	5.00	Sme, Ilt, Chl
2	Regolith	8.3	17.1	2.3	5.68	5.00	Sme, Ilt, Chl
3	Regolith	7.9	17.2	2.7	5.72	4.96	Sme, Ilt, Chl
4	Regolith	8.1	17.3	4.3	5.72	5.00	Sme, Ilt, Chl
6	Regolith	6.9	15.1	3.9	5.45	4.98	I-S, Ilt, Chl
8	Regolith	7.5	16.9	5.3	5.57	4.98	I-S, Ilt, Chl
9	Regolith	-	16.9	3.4		5.0	Sme, Ilt, Chl
Laguna Canapa							
12	Detrital	8.1	15.2	3.2	5.42	4.95	I-S, Ilt, Chl
13	Detrital	8.9	15.7	3.4	5.54	4.97	I-S, Ilt, Chl
14	Detrital	8.7	16.0	3.2	5.65		I-S, Ilt
15	Detrital	8.5	15.6	3.3	5.20	4.97	I-S, Ilt, Chl
16	Detrital	8.7	15.7	3.9	5.56	5.00	I-S, Ilt, Chl
17	Detrital	8.7	17.2	2.9		5.00	Sme, Ilt, Chl
18	Detrital	7.6	14.4	3.5	5.20	4.97	I-S, Ilt, Chl
19	Detrital	8.7	16.1	3.5		4.96	I-S, Ilt, Chl
24	Detrital	8.6	17.2	2.2	5.68	4.98	Sme, Ilt, Chl
26	Regolith	6.7	15.4	3.4	5.41	4.98	I-S Ilt, Chl
Laguna Hedionda							
28	Authigenic	8.7	16.4	3.9			Sme*, Ker
29	Authigenic	8.6	17.3	3.5			Sme, Ker
30	Detrital	8.8	15.6	3.2	5.23	5.00	I-S, Ilt
31	Detrital	8.7	16.0	2.9			I-S, Ker
35	Regolith	8.6	15.3	3.0	5.33	5.00	I-S, Ilt
Laguna Ramaditas							
37	Detrital	8.5	16.1	2.9			I-S, Ker
38	Detrital	9.0	15.6	3.3			I-S, Ker
41	Authigenic	-	14.8	3.6			Sme*, Ker
42	Authigenic	8.6	16.5	5.7			Sme*, Ker
43	Authigenic	6.8	16.1	4.9			Sme*, Ker
44	Authigenic	8.1	15.3	6.2			Sme*, Ker
45	Authigenic	7.9					Ker
Laguna Honda							
46	Authigenic	7.5	15.6	5.2			Sme*, Ker
49	Authigenic	7.8	16.3	3.7			Sme*, Ker
50	Authigenic	7.9	17.3	2.4			Sme, Ker
51	Authigenic	8.3	16.1	5.0			Sme*, Ker
52	Authigenic	8.0	16.9	4.2			Sme, Ker
Laguna Chiar Khota							
58	Authigenic	8.0	16.3	3.7			Sme*, Ker
59	Authigenic	7.7	16.4	6.0			Sme*, Ker
60	Authigenic	7.6	16.5	3.8			Sme*, Ker

https://doi.org/10.1007/s42860-020-00065-x Published online by Cambridge University Press

Table 3. (continued)

ID	Sediment Class	pH	d_{100} spacing (glycol)	(001) β_i	19–21°2θ *d* spacing (glycol)		Clay minerals
			Å	°2θ	Å	Å	
61	Authigenic	7.9	16.9	3.8			Sme, Ker
62	Authigenic	7.5	16.7	4.1			Sme*, Ker
63	Authigenic	7.8	17.0	4.4			Sme, Ker
64	Authigenic	7.7	17.2	3.7			Sme, Ker
65	Authigenic	7.8	15.7	8.5			Sme*, Ker
66	Authigenic	7.7	16.7	4.1			Sme*, Ker
67	Authigenic	7.8	16.7	3.1			Sme*, Ker
68	Authigenic	7.9	15.9	6.3			Sme*, Ker
69	Authigenic	7.8	15.4	8.4			Sme*, Ker
70	Authigenic	-	17.0	5.8			Sme, Ker
71	Authigenic	7.6	17.6	4.0			Sme, Ker
72	Authigenic	7.5	17.4	4.2			Sme, Ker
73	Authigenic	7.5	15.7	4.2			Sme*, Ker
74	Authigenic	7.7	16.1	4.7			Sme*, Ker
75	Authigenic	7.7	16.3	7.1			Sme*, Ker
76	Authigenic	8.0	16.7	5.0			Sme*, Ker
77	Authigenic	7.8	16.8	3.7			Sme, Ker
78	Authigenic	7.3	16.4	3.7			Sme*, Ker
79	Authigenic	7.3	15.1	10.5			Sme*, Ker
Laguna Chulluncani							
83	Detrital	8.4	17.2	3.7		5.00	Sme, Ilt
84	Detrital	8.5	17.1	3.3	5.52	5.00	I-S, Ilt
85	Detrital	8.0	15.9	3.6	5.22	4.98	I-S, Ilt
89	Detrital	8.4	15.8	3.8		5.00	I-S, Ilt
Clay Mineral References and Source Clays							
K-Hectorite		na	17.1	1.5	5.60		Sme
SHCa-1 Hectorite		na	16.8	1.3	5.59		Sme
SWa-1 Fe-Smectite		na	16.8	0.9	5.62		Sme
Nontronite, WA		na	16.9	1.1	5.64		Sme
Nontronite, PA		na	16.9	0.9	5.60		Sme
Saponite		na	17.0	0.7	5.65		Sme
Bentonite, SPC		na	17.0	1.1	5.65		Sme
Bentonite volclay		na	17.1	0.8	5.65		Sme
API no. 25 Mnt.		na	17.0	0.8	5.65		Sme
Mnt (AR)		na	17.1	0.9	5.60		Sme
Mnt (MS)		na	17.0	0.9	5.59		Sme

* Peak parameters for the (001) reflection were measured on glycolated smectite peaks ~6°2θ. Sme = smectite; Sme* = low-swelling smectites; Ilt = illite; I-S=interstratified illite-smectite; Chl = chlorite; Ker = kerolite; and Mnt = montmorillonite.

1-Regolith. XRD patterns for the glycolated regolith clay fractions all contain a low-angle reflection (15.1 to 17.3 Å) indicative of smectite or interstratified illite-smectite (I-S), discrete illite (10 Å and 5.0 Å), and a ~7.2 Å peak, probably from chlorite with weak (001) and (003) reflections given the arid environment (Fig. 2a). Interstratified clays were identified based on irrational basal spacings and a glycolated d_{001} spacing <16.9 Å that collapsed to 10 Å with heat treatment (400°C) (Table 3) (Moore and Reynolds 1989). When the (002/003) I-S peak could be resolved, most samples were estimated to have

https://doi.org/10.1007/s42860-020-00065-x Published online by Cambridge University Press

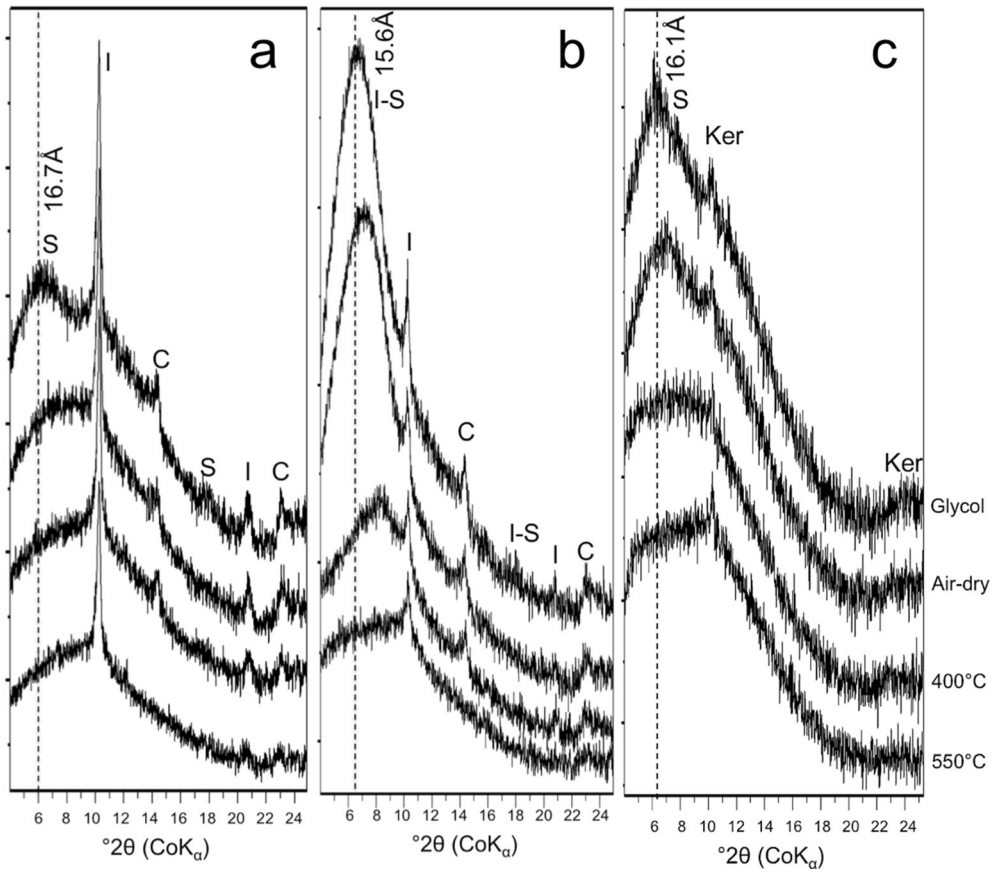

Fig. 2. Representative XRD patterns from the oriented <2 μm fraction samples after glycolation, air-drying, 400°C, and 550°C treatments for: (a) REG-1 representing regolith clay minerals. Regolith clay samples are composed of smectite (S) with varying degrees of interstratification with illite, discrete illite (I), and chlorite (C); (b) for CAN-15 representing detritus-rich mudflat samples. Detritus-rich mudflat clay samples are composed of smectite (S), illite-smectite (I-S), illite (I), and chlorite (C); and (c) RAM-43 representing authigenic mudflat samples. Authigenic clay samples are composed of smectite (S) characterized by high layer charge and kerolite (Ker)

between 20 and 50% randomly interstratified illite layers. These regolith sediments represent basin filling Quaternary alluvium.

2-Detrital. The majority of the XRD patterns from glycolated samples of the detritus-rich mudflat sediments were similar to the regolith clay patterns which showed detritus-rich mudflat sediment containing low-angle reflections with glycolated d_{001} spacings ranging from 14.4 to 17.2 Å mixed with discrete illite and chlorite (Table 3) (Fig. 2b). The percentage of illite interstratification, estimated from the (002/003) I-S reflections, ranged from 30 to 80%. This increase in illite interstratification indicated a general increase in layer charge compared to the regolith clays common with diagenetic alteration in saline or alkaline solutions (Deocampo et al. 2010; Hugettt et al. 2016). Discrete illite was not present in the XRD patterns from samples 31, 37, and 38 (sampled from below the sediment–water interface); instead they contained a broad, asymmetric shoulder at 10 Å resembling kerolite (Table 3) (Brindley et al. 1977; Léveillé et al. 2002).

3-Authigenic. Authigenic mudflat sediments produced oriented XRD patterns significantly different from the regolith and detrital-rich mudflat sediments. All of the XRD patterns from glycolated samples displayed a very broad, low-angle reflection that swelled with ethylene glycol and either collapsed with heat (400°C) treatment or was destroyed (Fig. 2c). The *d* spacings for the glycolated, low-angle reflections ranged from 14.8 to 17.6 Å (Table 3). These clays were identified as poorly formed, low-swelling smectite indicative of high layer charge materials with some illite-like layers based on the broad reflections and lack of a 10 Å peak with heat treatment (Deocampo et al. 2010). The only other features present (aside from micron-sized calcite) were weak peaks at 10 Å and 4.5 Å that did not swell with ethylene glycol and resembled kerolite (Brindley et al. 1977; Léveillé et al. 2002). Aside from the reduced *d*-spacings of the (001) peak for some samples, higher-angle reflections indicative of I-S or kerolite-stevensite interstratification were not observed in the XRD patterns. The samples extracted from the sediment–water interface under the surface water (Nos. 44, 45, and 79) exhibited XRD patterns for glycolated samples dominated by broad reflections consistent with biogenic silica.

https://doi.org/10.1007/s42860-020-00065-x Published online by Cambridge University Press

Due to interferences in the XRD patterns from diatom frustules and the broad 10 Å shoulder from kerolite in many samples, the coherent scattering domain for the glycolated (001) smectite reflection could not be calculated accurately. Instead, the integral breadth (β_i) of the (001) smectite reflection was used as a proxy to compare the nature of the smectite clays between sediment classes and the Source Clays and clay references analyzed (Table 3; Fig. 3). Broadening of the (001) reflection, resulting in a higher β_i value, occurs when materials have limited coherent domains from small crystallite size and randomly interstratified layers (Martin de Vidales et al. 1991). Analysis of box and whisker plots of the β_i from (001) smectite reflections by sediment class revealed a systematic increase in both the overall broadness and range of the β_i measured from the reference Source Clays (used as a benchmark for well crystallized clay) to the Bolivian clays in the 3-Authigenic sediments (Fig. 3). The Source Clays had the smallest values for β_i, ranging from 0.6 to 1.5 with the lowest average ($\bar{x} = 1.0$), while the authigenic clays displayed the greatest range in values for β_i, 2.4–10.5, and the highest average ($\bar{x} = 5.0$). The β_i values of the regolith and detrital-rich mudflat clays were fairly similar, ranging from 2.1 to 3.9 ($\bar{x} = 3.0$) for the regolith samples and from 2.4 to 3.9 ($\bar{x} = 3.3$) for the detrital samples.

Visible and Near-Infrared Spectroscopy

The major absorption bands identified in the samples were located around 1410 nm (7092 cm^{-1}) from OH and H_2O overtones (OH_{2v} and H_2O_{2v}), 1910 nm (5236 cm^{-1}) from H_2O combinations ($H_2O_{v+\delta}$), 2210 nm (4525 cm^{-1}) from Al–OH combinations, and/or 2310 nm (4329 cm^{-1}) from Mg–OH combinations (Bishop et al. 1994, 2013). A flat, broad reflectance band between 2210 and 2310 nm was also observed in most of the mudflat samples characteristic of opal or hydrated silica (Fig. 4) (Milliken et al. 2008). This Si–OH feature was excluded from Figs. 5, 6, and 7 for clarity unless it was the most prominent feature in the reflectance spectra. Subtle shifts in the 1410 nm band (OH_{2v}), the position of which depends on the corresponding cation (Al, Mg, or Fe), could not be distinguished due to the presence of hydrated silica in all of the samples, which contributed a very broad absorption over the region (Bishop et al. 2013).

1-Regolith. Reflectance spectra of the regolith <2 μm fractions all contained diagnostic absorption bands for dioctahedral smectite located at 1414 nm (7072 cm^{-1}), 1908 nm (5241 cm^{-1}), and 2208 nm (4529 cm^{-1}) (Fig. 5). The absence of any Mg–OH absorptions suggested that most of the Mg^{2+} released from the weathering of pyroxene and hornblende in the regolith was not incorporated into the pedogenic smectite but, instead, contributed to Mg enrichment of the surface water and sediments in the salars. These Al-rich clays are available for transport into the mudflats of the salars.

2-Detrital. Reflectance spectra from the <2 μm fractions from detrital mudflat sediments were characterized by metal–OH absorption bands for both dioctahedral clay (Al–OH) at 2208 nm (4529 cm^{-1}) and trioctahedral clay (Mg–OH) at 2313 nm (4323 cm^{-1}) (Fig. 6). Spectral analysis revealed that these NIR data resembled montmorillonite-beidellite mixed with magnesite; bulk XRD patterns provided no evidence of magnesite, dolomite, or Mg-calcite, however. Samples 31, 37, and 38 were collected from beneath standing water and exhibited the broad absorption bands from hydrated silica, 2200–2300 nm and, in the case

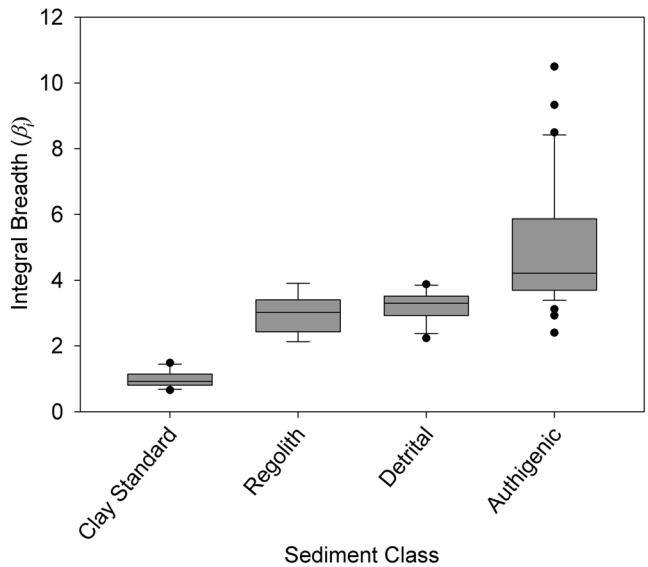

Fig. 3. Box and whisker plot of the integral breadth (β_i) of glycolated (001) smectite reflections from oriented <2 μm fraction XRD patterns by sediment class. The clay mineral Source Clays ($n = 11$) measured had the smallest β_i measured characteristic of large coherent scattering domains (Table 2); regolith ($n = 10$) and detrital ($n = 17$) clays had similar β_i, with detrital clays exhibiting slight broadening of the (001) reflection; Authigenic ($n = 33$) clays displayed the largest range and largest β_i characteristics of small coherent scattering domains from extremely small crystallite size and/or disorder

https://doi.org/10.1007/s42860-020-00065-x Published online by Cambridge University Press

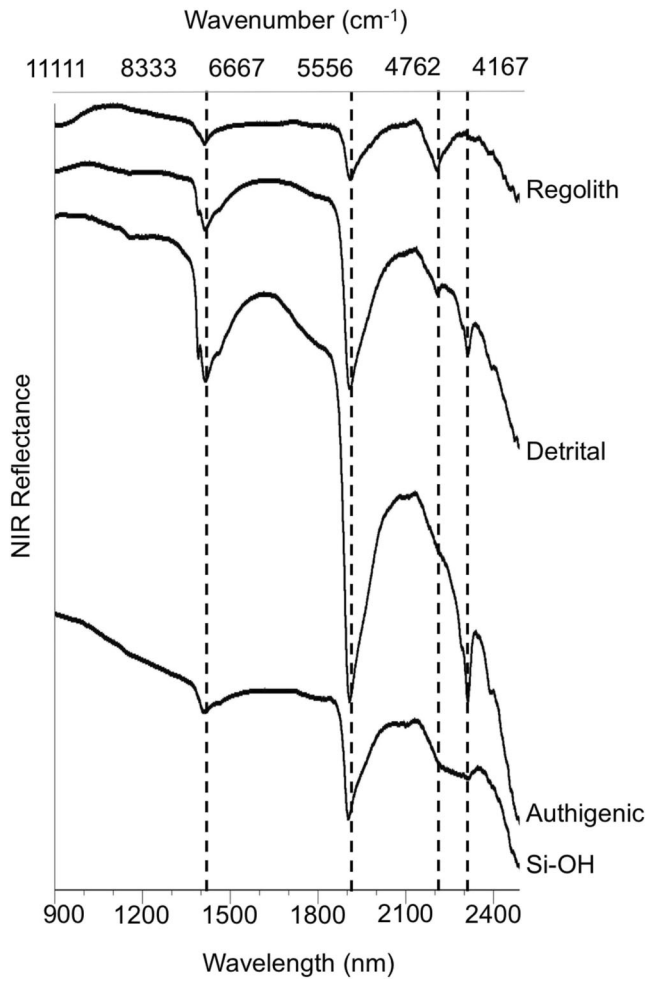

Fig. 4. Representative NIR reflectance spectra of the <2 μm fraction from each sediment class. The dotted lines identify the location of diagnostic absorption bands for clay minerals around 1410 nm (7092 cm^{-1}), 1910 nm (5236 cm^{-1}), 2210 nm (4525 cm^{-1}), and 2310 nm (4329 cm^{-1}). Regolith sediments from dry depression and slopes exhibit absorption bands for Al-dioctahedral smectite (2208 nm); detrital mudflat sediments with >10% detritus exhibit absorption bands for Al-dioctahedral smectite (2208 nm) and Mg-trioctahedral smectite (2313 nm); authigenic mudflat sediments with <10% igneous detritus exhibit absorption bands for Mg-trioctahedral smectite (2312 nm); sediments dominated by diatom frustules exhibit a broad absorption from hydrated silica (2200–2300 nm)

of 37 and 38, Mg–OH absorptions were absent. The clay minerals in the detrital-rich mudflat are a mix of detrital dioctahedral smectite and authigenic trioctahedral smectite. Substitution of Mg into the octahedral sheet (AlMg–OH) should shift the Al–OH band to higher wavelengths near 2212 nm (4520 cm^{-1}) but this was not observed, suggesting that the Al–OH and Mg–OH phases are distinct (Bishop et al. 2002a).

3-Authigenic. The NIR spectra of authigenic mudflat sediment displayed absorption features consistent with trioctahedral clay with the main absorption band located at 2312 nm (4325 cm^{-1}) from Mg–OH (Fig. 7). A broad feature was identified between 2200 and 2300 nm (4545–4348 cm^{-1}) in many of the samples and resembles hydrated silica. For samples 58, 60, and 74 the H_2O combination band at 1910 nm (5236 cm^{-1}) was shifted to longer wavelengths (1938–1942 nm) due to the presence of vegetation in the samples noted as green and pink algae in the field (Clark 1999). No evidence for Al–OH absorptions was observed in the NIR spectra, indicating that the dioctahedral clay from the regolith and detrital mudflat sediment is absent. Samples that were dominated by hydrated silica (42, 44, 45, 79) were fresh sediments sampled from under the surface water similar to the detrital sediment samples 31, 37, and 38.

Scanning Electron Microscopy

1-Regolith. Clay minerals separated from the regolith sediments displayed a mix of well defined, hexagonal, spherical, and platy minerals with small, flaky particles consistent with XRD results from dioctahedral smectite (montmorillonite or

https://doi.org/10.1007/s42860-020-00065-x Published online by Cambridge University Press

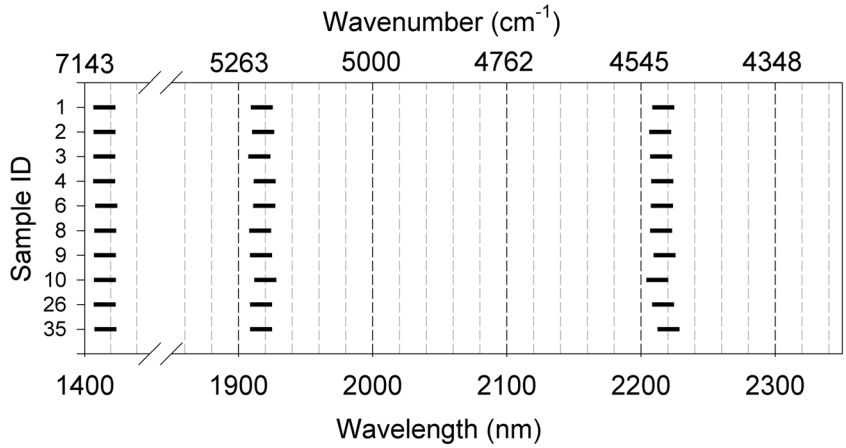

Fig. 5. Location of major absorption bands in the NIR reflectance spectra for the <2 μm fraction separated from regolith samples. Absorption bands are present at 1414 nm (7072 cm^{-1}) from OH_{2v} and H_2O_{2v} overtones, 1908 nm (5241 cm^{-1}) from $H_2O_{v+\delta}$ combination stretching, and 2208 nm (4529 cm^{-1}) from Al–OH combinations. All NIR spectra confirm that Al-dioctahedral smectite is the dominant clay mineral

beidellite), illite, and chlorite (Fig. 8a). The EDS spectra of the flaky particles with classic smectite textures confirmed that the clays are Al-rich (data not shown).

2-Detrital. The detrital-rich sediments displayed platy and spherical minerals similar to those present in the regolith, as well as poorly-preserved remnants of diatom fragments and flaky masses (Fig. 8b). Within the flaky masses, individual particles were still distinguished by their well defined edges.

3-Authigenic. The authigenic mudflat sediments are composed predominantly of diatom frustules with small platy particles mixed with fluffy aggregates (Fig. 8c–f). Within the authigenic sediments the diatom frustules display evidence of dissolution and coating/replacement with fine-grained material as the delicate morphology of the microfossils is obscured for many of the samples (Fig. 8c,d). The NIR reflectance spectra and EDS analysis (data not shown) confirmed that the fine-grained aggregates are rich in Mg and Si. The <2 μm wide

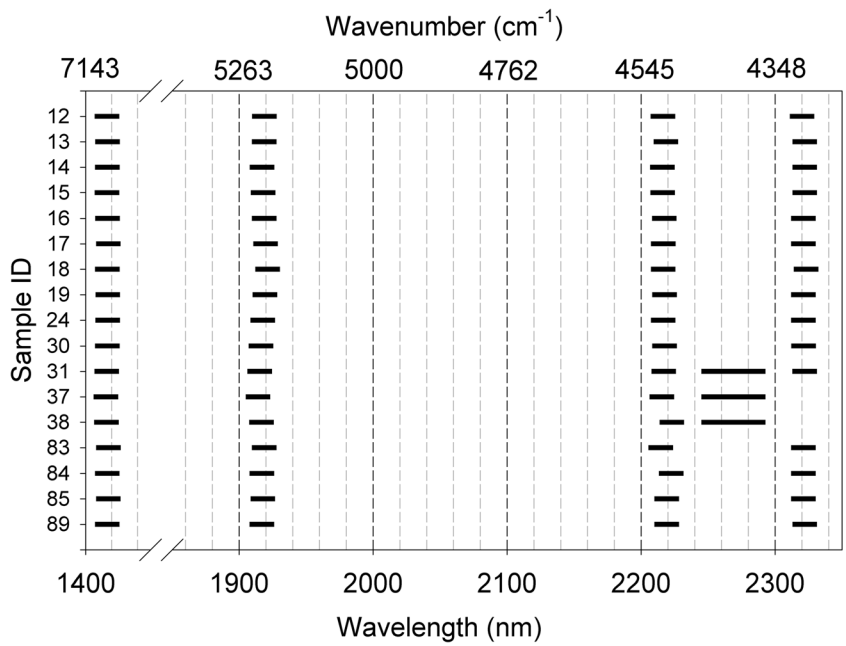

Fig. 6. Location of major absorption bands in the NIR reflectance spectra for the <2 μm fraction separated from detritus-rich mudflats samples. Absorption bands are present at 1415 nm (7067 cm^{-1}) from OH_{2v} and H_2O_{2v} overtones, 1910 (5236 cm^{-1}) from $H_2O_{v+\delta}$ combination stretching, 2208 nm (4529 cm^{-1}) from Al–OH combinations, and 2313 (4323 cm^{-1}) from Mg–OH combinations. The NIR spectra confirm that Al-dioctahedral smectite and Mg-trioctahedral smectite are present. Broad bands in the range 2200–2300 nm indicate biogenic silica

https://doi.org/10.1007/s42860-020-00065-x Published online by Cambridge University Press

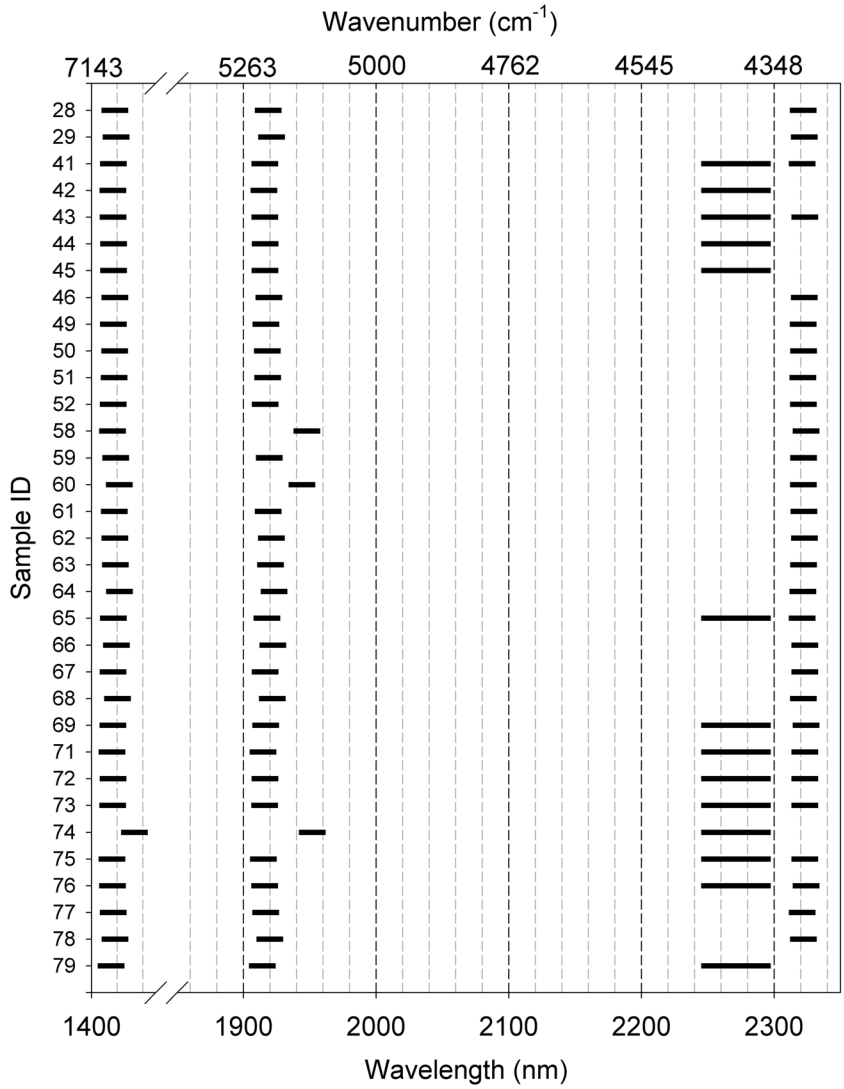

Fig. 7. Location of major absorption bands in the NIR reflectance spectra for the <2 μm fraction separated from authigenic mudflats samples. Absorption bands are present at 1414 nm (7072 cm^{-1}) from OH_{2v} and H_2O_{2v} overtones, 1910 nm (5236 cm^{-1}) from $H_2O_{v+\delta}$ combination stretching, and 2312 (4325 cm^{-1}) from Mg–OH combinations. The NIR spectra confirm Mg-trioctahedral smectite is the dominant clay mineral present. Broad bands between 2200–2300 nm designate indicate silica

scalenohedral crystals were of calcite, confirmed in the XRD spectra and EDS analysis of the grains (data not shown).

Samples taken from below the sediment–water interface (Nos. 42, 44, 45, 79) are composed of well preserved diatom frustules still displaying the delicate morphology of the stria and raphe on the porous structure (Fig. 8e,f). Sparse aggregates of fluffy masses are still present in these samples, representing poorly formed minerals. The dominance of diatom frustules within these sediments is consistent with the NIR spectra and XRD profiles, which exhibited a strong absorption for hydrated silica and a broad hump caused by amorphous material at 25°2θ. These samples represent the most recent sedimentary deposits from the salar, confirming that endogenic calcite and diatom frustules are the main materials settling out of the surface water, and that neoformed phyllosilicate minerals are not precipitating directly from solution in appreciable amounts. The fine-grained, fluffy material in the rest of the samples is a product of frustule dissolution and alteration rather than neoformed phyllosilicates.

Chemical Analysis

The Al:Fe:Mg ternary diagrams for selected <2 μm fractions (Fig. 9a) revealed a pattern of increasing Mg content from the regolith clays to the mudflat clays where: 1-Regolith < 2-Detrital < 3-Authigenic. These data are consistent with the NIR spectra for each sediment class where the regolith clays are dominated by Al-dioctahedral smectite and the authigenic clays are dominated by Mg-trioctahedral smectite. The Fe:K:Li ternary diagrams (Fig. 9b) showed that both the 1-Regolith and 2-Detrital clays contain greater amounts of Fe

https://doi.org/10.1007/s42860-020-00065-x Published online by Cambridge University Press

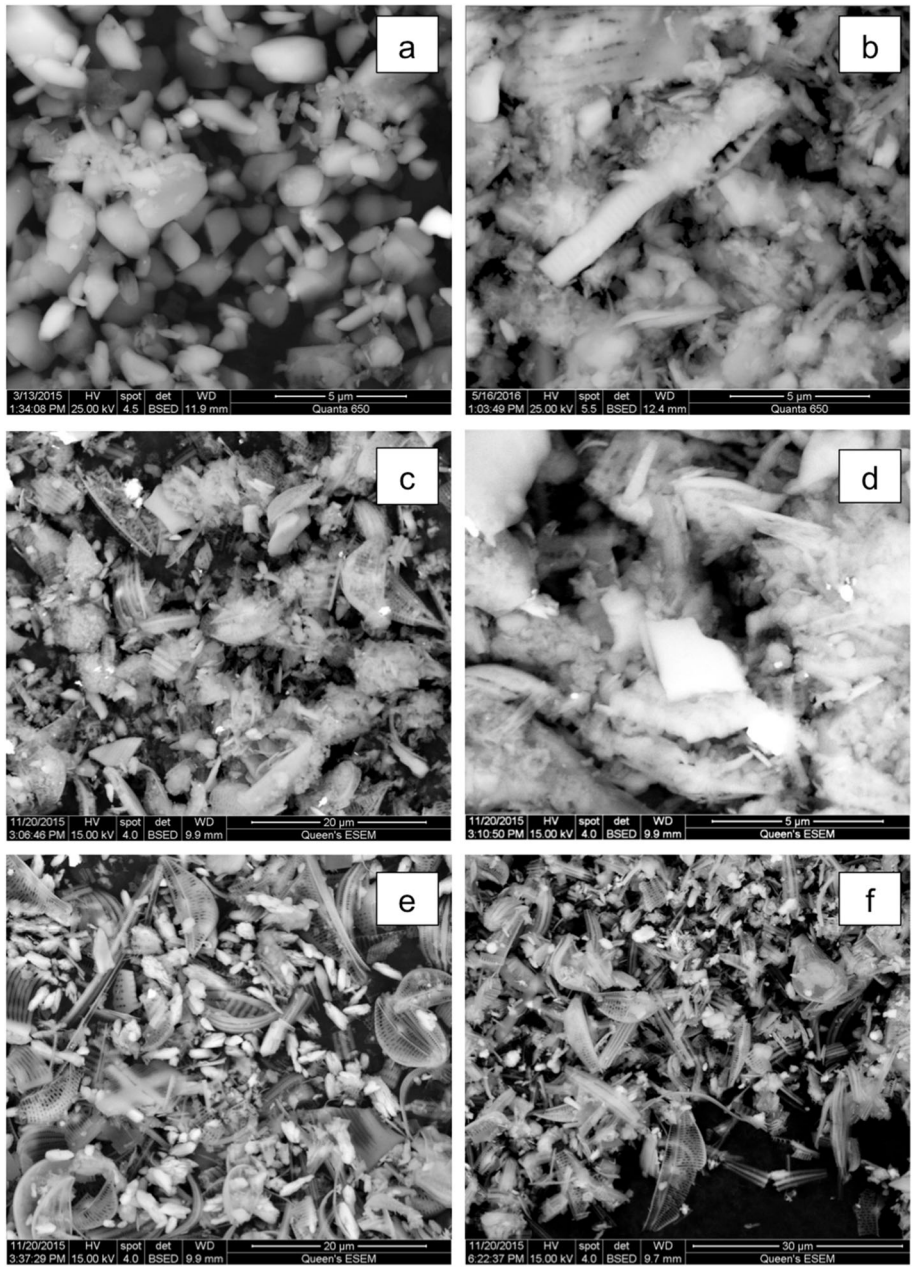

Fig. 8. Representative BSED-SEM images of the <2 µm fraction from each detrital class: (**a**) regolith clay samples display well defined particulates characteristic of weathering from igneous minerals; (**b**) detritus-rich mudflat samples display a mix of well defined particulates and conglomerated masses rich in Mg and Si from EDS data; (**c**-**d**) authigenic mudflat samples display poor–moderately well preserved diatom frustules and fluffy masses, rich in Mg and Si from EDS data; (**e**-**f**) authigenic detritus-poor mudflat samples taken from the sediment–water interface below the surface water display predominantly well-preserved diatom frustules. * Due to the low density of the diatom frustules (<0.12–0.25 g cm^{-3}) the large siliceous skeletons remained in suspension during the clay separation

(>60%) than of K and Li; some of the detrital clays displayed a slight increase in K, however, consistent with the increase in illite layers, or the decrease in the glycolated d_{001}, observed in the XRD patterns (Fig. 2b). The Mg-rich clays sampled from the 3-Authigenic sediments, conversely, displayed increasing concentrations of K and Li relative to Fe. Given the small, glycolated d_{001} spacings for many of the 3-Authigenic clays, K must be present as an interlayer cation contributing to illite-like layers deriving from the low-temperature illitization of smectite. The large Li concentrations in the 3-Authigenic clays could be from hectorite or Li-rich saponite/stevensite in the evaporative basin (Fig. 9b). Minor/trace elements and heavy metals were either below detection limits or enriched in specific salars with no apparent pattern to the sediment class and were not included, therefore.

https://doi.org/10.1007/s42860-020-00065-x Published online by Cambridge University Press

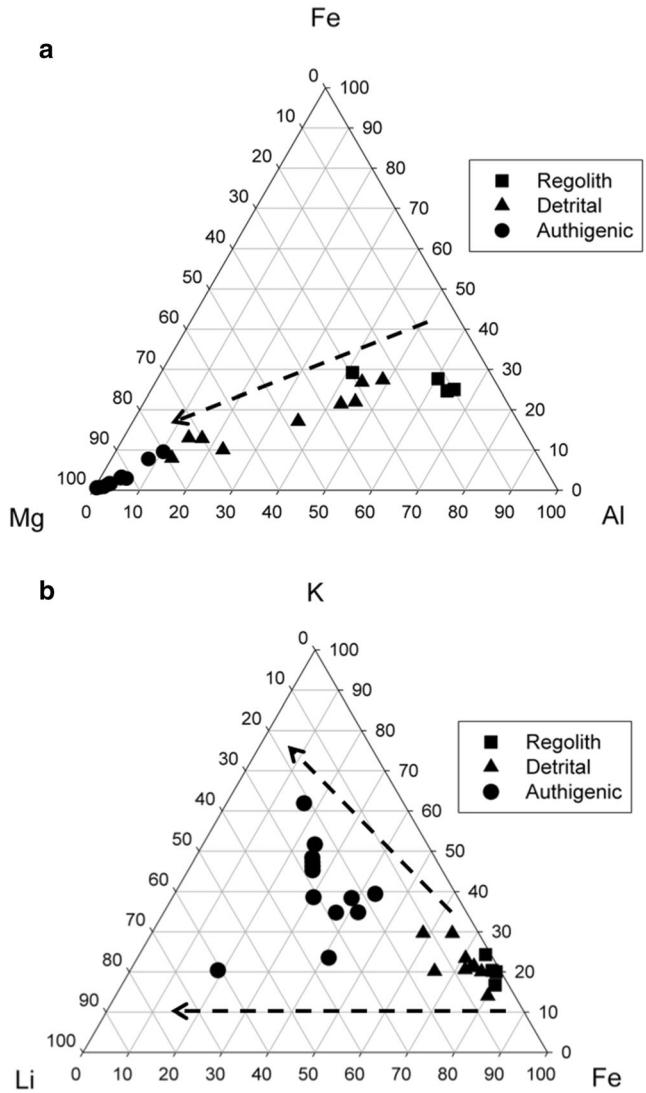

Fig. 9. Ternary diagrams of <2 μm fraction compositions separated from regolith sediments (squares), detritus-rich mudflat sediment (triangles), and authigenic mudflat sediments (circles). (**a**) The Al:Fe:Mg ternary diagram displays increasing Mg-enrichment within the mudflats where authigenic clays forming in detritus-poor environments are dominated by Mg-rich chemistries. (**b**) The Fe:K:Li ternary diagram displays increasing K and Li content in authigenic clays forming in detritus-poor environments

Water Chemistry

Surface-water chemistry data from studies published over the period 1983 to 2014 (and including the current study) were compiled to understand the range of geochemical conditions experienced within each salar (Badaut and Risacher 1983; Servant-Vildary and Roux 1990; Risacher and Fritz 1991; Dejoux 1993; Sylvestre et al. 2001) (Fig. 10). Even though the data span ~30 y and are highly variable, the general trend in the Mg:Si ratio of the surface water compared to the inflow water is consistent across studies. The variability in the data is expected for closed basins where ionic concentrations fluctuate with evaporation and depend on the time and season of sampling. Compared to inflow waters that are rich in dissolved Si (Mg:Si < 1), the surface waters of the salars are significantly enriched in Mg^{2+} with respect to dissolved Si (Mg:Si > 1) (Fig. 10). This Mg^{2+} enrichment is especially pronounced in HED, CHKT, and CHU where the mean Mg:Si ratios were 130, 98, and 73, respectively. Surface-water pH was also highly variable for all the salars over the 30 y period, fluctuating between neutral and alkaline for most salars, although the pH would depend on the season when sampling was carried out (i.e. wet vs dry) (Table 1; Fig. 11). For HED, RAM, and CHKT the pH values measured/reported were consistently < 8.5, which is the threshold consistently identified for Mg-silicate precipitation

https://doi.org/10.1007/s42860-020-00065-x Published online by Cambridge University Press

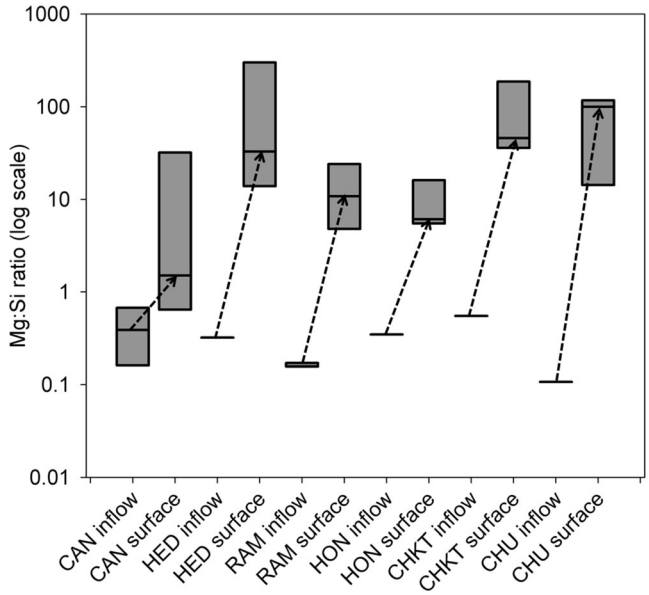

Fig. 10. Box and whisker plots of the Mg:Si ratio of inflow waters compared to salar surface waters from 1983–current study; (data from Badaut and Risacher 1983; Servant-Vildary and Roux 1990; Risacher and Fritz 1991; and Dejoux 1993). For all the salars, evaporative concentration of the inflow waters results in significant enrichment of Mg relative to Si in the surface waters of the salars

from solution (Badaut and Risacher 1983; Tosca et al. 2011; Tosca 2015).

DISCUSSION

1-Regolith. Clay minerals identified in the <2 μm fraction of regolith samples are consistent with illite, chlorite, and randomly interstratified I-S rich in Al-dioctahedral smectite. These samples were all characterized by Al–OH absorptions near 2208 nm (4528 cm^{-1}) in the NIR spectra, chemical composition dominated by Al, and low-angle reflections in the XRD data that swell with ethylene glycol treatment. This suite of dioctahedral phyllosilicates is expected from pedogenic weathering in the soils (regolith) surrounding the salars. Weathering of biotite, feldspar, pyroxene, and hornblende present in the surrounding andesites and rhyodacites has been shown to produce Al-rich phases while releasing Fe and Mg to

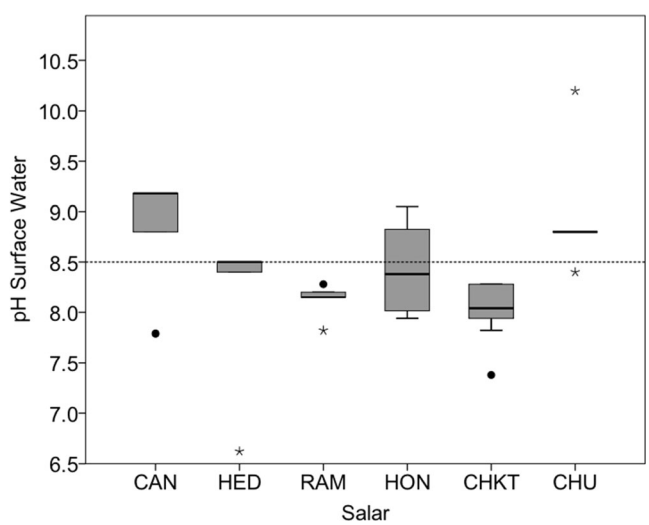

Fig. 11. Box and whisker plots displaying the range of pH values measured from surface water samples from each salar from 1983–current study; (data from Badaut and Risacher 1983; Servant-Vildary and Roux 1990; Risacher and Fritz 1991; Dejoux 1993; and Sylvestre et al. 2001). The salars range from neutral to alkaline over the years of study; however, the pH of HED, RAM, and CHKT has never increased above the threshold for Mg-silicate neoformation despite the evidence of Mg-smectite within the mudflats of these salars

https://doi.org/10.1007/s42860-020-00065-x Published online by Cambridge University Press

solution (Hover and Ashley 2003; Deocampo et al. 2009). Clay minerals formed via weathering of detrital minerals also tend to have larger crystallite sizes and produce sharper reflections in XRD, both of which were observed for the regolith clays. These dioctahedral phyllosilicates represent potential detrital sources for clay minerals entering the salars.

2-Detrital. Clay minerals in the detritus-rich mudflats are a mix of detrital (illite, chlorite, and I-S-rich in Al-dioctahedral smectite) and authigenic (Mg-smectite) phyllosilicates. All detritus-rich mudflat sediments displayed absorptions from both Al–OH (2208 nm; 4528 cm^{-1}) and Mg–OH (2313 nm; 4323 cm^{-1}) combinations in the NIR spectra with an overall shift toward Mg-rich chemistries compared to the 1-Regolith clays. The XRD patterns also exhibited evidence of broadening of the glycolated (001) reflections and increased layer charge (smaller glycolated *d* spacings) of the smectite minerals compared to the regolith smectite clays. Without any shifts in the Al–OH band to higher wavelengths near 2212 nm (4520 cm^{-1}) signifying Mg–OH contributions, these observations suggest that authigenic Mg-smectite is forming on, or replacing, dioctahedral smectite within the mudflats. The authigenic clay minerals are characterized by small crystallite sizes, structural disorder, and high layer charge consistent with low-temperature illitization due to increasing octahedral Mg in the saline environment evident in the broad, asymmetric reflections and Mg content of the minerals (Figs. 2, 3, and 9). Similar broadening of the (001) reflection was measured by Cuevas et al. (2003) who used peak deconvolution analysis to conclude that combining a broad 18 Å reflection from authigenic stevensite with a sharper 17 Å reflection from detrital dioctahedral smectite would produce the broad reflections observed. The transformation of detrital Al-dioctahedral smectite to authigenic Mg-trioctahedral smectite has been demonstrated in Abert Lake, Oregon (Jones and Weir 1983; Banfield et al. 1991); in Miocene lacustrine units in the Madrid basin, Spain (Bellanca et al. 1992); in the Salina Ometepec, Baja, California (Hover et al. 1999); in Neogene Vicalvaro deposits, Madrid, Spain (Cuevas et al. 2003); in Lake Eyasi and Ngorongoro Crater, Tanzania (Hover and Ashley 2003; Deocampo 2005); and in the Pliocene Olduvai Gorge, Tanzania (Deocampo et al. 2009). The process of the transformation has been theorized by several studies and includes: topotactic growth of Mg-rich layers onto existing detrital clays producing di- and tri-octahedral crystals, complete dissolution of Al-dioctahedral smectite and re-precipitation of Mg-trioctahedral smectite, and solid state transformation of dioctahedral clays to trioctahedral clays producing coexisting domains within the same sheet or an intermediate composition of the octahedral sheet (Banfield et al. 1991; Cuevas et al. 2003; Hover and Ashley 2003; Deocampo et al. 2009). Due to the lack of evidence for octahedral substitution of Mg for Al in the NIR reflectance spectra (i.e. distinct bands for Al–OH and Mg–OH), the most likely process for authigenic clay formation in Bolivia appears to be topotactic growth of the Mg-rich phases onto existing Al-rich phases.

3-Authigenic. Clay minerals in the authigenic sediments are consistent with Mg-smectite (probably stevensite or saponite), and kerolite forming on/replacing diatom frustules. The enrichment of Li in the authigenic clays in CHKT could indicate that hectorite is forming; however, analytical electron microscopic analysis coupled with transmission electron microscopic analysis (AEM/TEM) of individual clay particles would be required to establish if enough Li is present in any individual particles to identify them as hectorite. If hectorite were present, however, a shift in the trioctahedral combination band to 2306 nm (4335 cm^{-1}) should be observed but was not (Bishop et al. 2002b). The NIR spectra for these sediments are dominated by hydrated silica and/or Mg–OH absorptions (2312 nm; 4325 cm^{-1}). X-ray diffraction analyses produced very broad basal reflections the positions of which changed with ethylene glycol treatment and weak reflections from kerolite (10 and 4.5 Å). Broad basal reflections are indicators of authigenic formation for clay minerals (Deocampo et al. 2009, 2010). Within the mudflats, kerolite is precipitating from the Mg^{2+} -enriched solutions, characterized by an excessively high Mg^{2+}/SiO_2 activity ratio, which leach through the diatomaceous sediment (Galán and Pozo 2011; Tosca and Masterson 2014). Subsequent removal of Mg^{2+} via kerolite precipitation shifts the solutions into the stability field of stevensite, allowing the smectite to precipitate (Galán and Pozo 2011; Tosca and Masterson 2014).

The samples that exhibited glycolated d_{001} spacings of <17 Å are consistent with a high octahedral layer charge coupled with moderate K^+ fixation (Deocampo et al. 2009). A similar precursor smectite was described in the Tagus basin (Spain) that had variable interlayer spacings (10–18 Å) and a high layer charge from deficiencies in the octahedral cations (Santiago de Buey et al. 2000). The absence of I-S interstratification in the XRD data could be due to incomplete K^+ fixation in the Na-rich solutions. Deocampo et al. (2009) suggested layer-charge increases and K^+ fixation are decoupled, and that K^+ fixation occurs under freshwater conditions when the K/Na ratio is higher. The rest of the Mg-rich samples that swelled to ~17 Å resemble authigenic kerolite-stevensite similar to the clays from palustrine environments from the Neogene Madrid basin (Spain) (Pozo and Casas 1999). The Neogene kerolite is thought to have originated via precipitation from solution or a gel-like medium (neoformation) based on the colloform texture, chemical purity, and XRD reflections; while early diagenetic processes (increasing salinity via evaporation and drying) converted the kerolite to kerolite-stevensite prior to pure stevensite formation (Pozo and Casas 1999). Although diatoms were not included in the observations by Pozo and Casas (1999) diatomaceous marls are present in the Miocene sediments of the Madrid basin, indicating the green algae could be affecting the mineral assemblages present (Bellanca et al. 1992).

The replacement of biogenic silica with Mg-smectite is consistent with the observations of Badaut and Risacher

https://doi.org/10.1007/s42860-020-00065-x Published online by Cambridge University Press

(1983) who reported stevensite replacing diatom frustules in water samples when the pH was above >8.5 in the same salars as the present study; the pervasiveness of the diatom frustules throughout the mudflats (~1 m of diatomaceous sediment) has not been reported previously, however. Authigenic smectite formation within the mudflats, however, was not restricted by the pH of the surface water as found by Badaut and Risacher, (1983) because all of the sediments exhibited evidence of phyllosilicate formation due to the concentration of solutes within the pore fluids. The mudflats adjacent to saline lakes are dynamic environments subject to periodic wet/dry cycles and strong capillary forces that concentrate solutes, especially Mg^{2+} after calcite and gypsum precipitation.

Widespread evidence of sepiolite was absent in the XRD patterns and NIR reflectance spectra despite the silicate-rich, brackish environments expected to favor the neoformation of sepiolite from evaporating waters. Direct precipitation of sepiolite from solution has been assumed previously in the dolomitic sepiolite beds of the Amargosa Flat playa, Nye County, Nevada (Papke 1972), in the Allou Kagne deposit, Senegal (García-Romero et al. 2007), and in the Serinhisar-Acipayam basin, Turkey (Akbulut and Kadir 2003). Based on the Mg:Si ratios measured during the past 30 y, waters within the salars clearly become significantly enriched in Mg, but not silica, during evaporative concentration. From SEM analysis of the authigenic mudflat sediments not obscured by detritus, evidence is clear that these sediments are dominated by diatom frustules. Diatoms are capable of surviving under wide ranges of salinities and pH, and effectively remove silica from the water column via biologically mediated uptake to form their siliceous skeletons (DeMaster 2003). The ultimate fate of the silica depends on silica solubility and the geochemical conditions present following the death of the biota: i.e. preservation vs dissolution. Factors that affect silica solubility and diatom dissolution have been summarized by Hecky and Kilham (1973); DeMaster (2003), Ryves et al. (2006), Flower and Ryves (2009), Loucaides et al. (2012), and Tutolo and Tosca (2018) and include:

- pH: dissolution increases with increasing pH, due to deprotonation of silanol groups that helps promote hydrolysis of the siloxane bonds, especially above pH >9 where dissolution increases exponentially; the pKa for silicic acid at 25°C is 9.8.
- Temperature: The rate of frustule dissolution increases linearly with increasing temperature from 4 to 30°C.
- Salinity: alkali salts increase frustule dissolution until solutions become hypersaline; further increases in salinity decrease silica solubility, especially when divalent cations are present (Ca^{2+}, Mg^{2+}, and Fe^{2+}).
- Depth of the water column: a deeper water column allows more time for the frustules to dissolve before sedimentation. In deep lakes and ocean environments, many diatoms dissolve within the water column before settling.
- Sinking velocities: the sinking velocity is affected by the size (dependent on the nutrient status of the water) and aggregation of diatom cells where larger cells/groups sink faster, allowing less time for dissolution.
- Al incorporation: soluble Al present during diatom growth can be incorporated into the siliceous skeleton and ultimately decreases the solubility of the frustules.

In the Bolivian salars, temporal variations in the neutral-alkaline solutions and brackish-hypersaline conditions create a range of biogeochemical conditions within each salar and between salars. For most of the salars, however, the slightly alkaline waters (pH <9), cold temperatures (0–10°C), and shallow water depths (<30 cm) that promote rapid rates of sedimentation act to slow the dissolution of biogenic silica. These conditions promote the preservation of diatom frustules, especially in HED, RAM, and CHKT where silica is removed from solution and cannot contribute to authigenic sepiolite formation. Under more optimal conditions for dissolution, Michalopoulos et al. (2000) measured the complete conversion of diatom frustules to aluminosilicate clays in 23 months. In the Bolivian salars, conversely, the sedimentation of the frustules has built-up diatomaceous muds >1 m thick in some of the salars. Instead of dissolving in the water column, the deposited frustules become a slow-release source of Si as Mg-rich fluids leach through sediment pores allowing kerolite and Mg-smectite to form during evaporative concentration in the mudflats. Samples from the current study included transects across the mudflats of the salars; however, samples were not taken where inflowing waters mix with surface waters. Deposits of sepiolite might be present where Si-rich inflow waters react with saline solutions in the salars before silica uptake by the diatoms occurs.

Instead of neoformation (precipitation from solution), in many other basins sepiolite seems to form from the dissolution of trioctahedral Mg-smectite, within soils and lake margins, and from the dissolution of dolomite (Chahi et al. 1997; Galán and Pozo 2011). In sediments from the Jbel Rhassoul, Morocco, sepiolite was found replacing neoformed stevensite during climatic periods characterized by low salinity and high concentrations of dissolved silica from fresh water entering the basin (Chahi et al. 1997). In the Ahiler area of the Eskişehir sepiolites, Turkey, late-stage diagenetic events caused the dissolution of dolomite, and diatomites favored the formation of sepiolite (Ece and Çoban 1994). In the Madrid basin (Spain), weathering of granites and the dissolution of siliciclastic grains during calcretization in alluvial fans produced Si- and Mg-enriched groundwater that led to the precipitation of sepiolite followed by opal within the detrital lake sediments (Bustillo and Bustillo 2000). Additionally, in the Vicalvaro sepiolite deposit, Madrid Neogene Basin, Spain, sepiolite initially interpreted to have formed via neoformation by precipitation is now interpreted as forming from the diagenetic alteration of Mg-rich smectite (Cuevas, et al. 2003; Pozo and Calvo 2018). In the Sariyer Formation (Turkey), the Intermediate Unit in the Madrid basin (Spain), and the Tuzgölü basin (Turkey), sepiolite-palygorskite were found replacing dolomite during dry periods coupled with sulfide

https://doi.org/10.1007/s42860-020-00065-x Published online by Cambridge University Press

oxidation in the presence of disordered silica (Kadir et al. 2010; Gürel and Özcan 2016). In all of these cases, sepiolite-palygorskite apparently may be restricted to subsurface environments and post-depositional alteration of Mg-smectite and dolomite. In subsurface environments (pore fluids of detrital mudflats, soils, and deltas) the sunlight required for algal growth is absent, which inhibits the growth of diatoms and allows dissolved Si concentrations to increase and sepiolite-palygorskite to precipitate. For the Bolivian salars, post-depositional alteration could convert the smectites in the mudflats to sepiolite if freshwater conditions returned or dissolved silica increased significantly.

CONCLUSIONS

Clay minerals forming on the Bolivian Altiplano follow a pattern of increasing Mg-enrichment from detrital, Al-dioctahedral phyllosilicates to authigenic, Mg-trioctahedral phyllosilicates transforming detrital clays and diatom frustules. Despite the range of geochemical environments across the salars, from brackish to hypersaline and neutral to alkaline, all of the authigenic clays forming are kerolite or Mg-smectite, probably stevensite. The pH of evaporating solutions defines an important threshold for the neoformation of clays from solution at pH 8.5 (both sepiolite and Mg-smectite); however, the Mg:Si ratio of the pore solutions has a greater impact on the mineralogy of the clays that are forming. Very high Mg:Si ratios favor kerolite, especially in detritus-poor sediments, while decreasing Mg:Si ratios favor Mg-smectite. Authigenic clays in the mudflats are all characterized by high layer charge, small crystallite sizes, and/or stacking disorders producing very broad, low-angle X-ray reflections. Aside from evaporites and phyllosilicates, the mudflats are dominated by diatom frustules, explaining the depletion of dissolved Si in the evaporating waters compared to the inflowing waters. Diatomaceous sediments >1 m thick have accumulated due to slow rates of diatom dissolution as a result of cold temperatures, shallow water depths, salinity, and neutral–slightly alkaline pH solutions. This removal of Si from solution by diatoms prevents sepiolite formation, which requires high concentrations of dissolved Si. In modern sediments, the activity of diatom frustules may even restrict sepiolite-palygorskite to subsurface environments where sunlight is absent and diatom growth is inhibited, thereby allowing dissolved Si to accumulate in the pore fluids. Burial of the Bolivian mudflat sediments could favor the conversion of smectite to sepiolite as the diatom frustules will act as a source of silica during potential, future, epigenetic and diagenetic reactions. Overall, the control of Si concentrations in solution by diatoms has a large impact on the types of clay minerals that will form, and may have been underestimated when analyzing ancient sediments.

ACKNOWLEDGMENTS

Many thanks to the Analytical Services Unit at Queen's University for the chemical analysis by ICP-OES. The authors are very grateful to James Amonette from Pacific Northwest National Laboratory and Michael Thompson from Iowa State University for the clay mineral references. They also thank Jenny Huggett, Benjamin Tutolo, an anonymous reviewer, and the Editor-In-Chief, Joseph Stucki, for helpful and constructive comments. Field guides, Nelson and Marie from Betto Tours in Uyuni, Bolivia, are thanked for helping to navigate the southern Altiplano. This research was supported by the Mineralogical Association of Canada Travel Grant, the Marie Mottashed Graduate Scholarship, and an NSERC Discovery Grant to R. Peterson.

REFERENCES

Akbulut, A., & Kadir, S. (2003). The geology & origin of sepiolite, palygorskite, & saponite in Neogene lacustrine sediments of the Serinhisar-Acipayam basin, Denizli, SW Turkey. *Clays & Clay Minerals, 3*, 279–292.

Allmendinger, R. W., Jordan, T. E., Kay, S. M., & Isacks, B. L. (1997). The evolution of the Altiplano-Puna plateau of the Central &es. *Annual Review of Earth & Planetary Science, 25*, 139–174.

Argollo, J., & Mourguiart, P. (2000). Late Quaternary climate history of the Bolivian Altiplano. *Quaternary International, 72*, 37–51.

Badaut, D., & Risacher, F. (1983). Authigenic smectite on diatom frustules in Bolivian saline lakes. *Geochimica et Cosmochimica Acta, 47*, 363–375.

Banfield, J. F., Jones, B. F., & Veblen, D. R. (1991). An AEM-TEM study of weathering & diagenesis, Abert Lake, Oregon: 2. Diagenetic modification of the sedimentary assemblage. *Geochimica et Cosmochimica Acta, 55*, 2795–2810.

Bellanca, A., Calvo, J. P., Censi, P., Neri, R., & Pozo, M. (1992). Recognition of lake-level changes in Miocene lacustrine units Madrid basin, Spain. Evidence from facies analysis, isotope geochemistry & clay mineralogy. *Sedimentary Geology, 76*, 135–153.

Birsoy, R. (2002). Formation of sepiolite-palygorskite & related minerals from solution. *Clays & Clay Minerals, 50*, 736–745.

Bishop, J. L., Pieters, C. M., & Edwards, J. O. (1994). Infrared spectroscopic analysis on the nature of water in montmorillonite. *Clays & Clay Minerals, 42*, 702–716.

Bishop, J., Madejová, J., Komadel, P., & Fröschl, H. (2002a). The influence of structural Fe, Al & Mg on the infrared OH b&s in spectra of dioctahedral smectites. *Clay Minerals, 37*, 607–616.

Bishop, J., Murad, E., & Dyar, M. D. (2002b). The influence of octahedral & tetrahedral cation substitution on the structure of smectites & serpentines as observed through infrared spectroscopy. *Clay Minerals, 37*, 617–628.

Bishop, J. L., Rampe, E. B., Bish, D. L., Abidin, Z., Baker, L. L., Matsue, N., & Henmi, T. (2013). Spectral & hydration properties of allophane & imogolite. *Clays & Clay Minerals, 61*, 57–74.

Bowen, B. B., & Benison, K. C. (2009). Geochemical characteristics of naturally acid & alkaline saline lakes in southern Western Australia. *Applied Geochemistry, 24*, 268–284.

Brindley, G. W., Bish, D. L., & Wan, H.-M. (1977). The nature of kerolite, its relation to talc & stevensite. *Mineralogical Magazine, 41*, 443–452.

Bristow, T. F., & Milliken, R. E. (2011). Terrestrial perspective on authigenic clay mineral production in ancient Martian lakes. *Clays & Clay Minerals, 59*, 339–358.

Bustillo, M. A., & Bustillo, M. (2000). Miocence silcretes in argillaceous playa deposits, Madrid basin, Spain: petrological & geochemical features. *Sedimentology, 47*, 1023–1037.

Cabrol, N. A., Grin, E. A., Chong, G., Minkley, E., Hock, A. N., Yu, Y., Bebout, L., Fleming, E., Häder, D. P., Demergasso, C., Gibson, J., Escudero, L., Dorador, C., Lim, D., Woosley, C., Morris, R. L.,

Tambly, C., Gaete, V., Galvez, M. E., Smith, E., Uskin-Peate, I., Salazar, C., Dawidowicz, G., & Majerowicz, J. (2009). The high-lakes project. *Journal of Geophysical Research: Biogeosciences, 114*, G00D06. https://doi.org/10.1029/2008JG000818.

Calvo, J.P., Blanc-Valleron, M.M., Rodrigue-Ar&ia, J.P., Rouchy, J.M., & Sanz, M.E. (1999). Authigenic clay minerals in continental evaporitic environments. Pp 129–151 in: *Paleoweathering, Paleosurfaces & Related Continental Deposits* (M. Thiry & R. Simon-Coincon, editors). Special Publication of the International Association of Sedimentologists, *27,* Blackwell Sciences, Oxford, UK.

Chahi, A., Fritz, B., Duplay, J., Weber, F., & Lucas, J. (1997). Textural transition & genetic relationship between precursor stevensite & sepiolite in lacustrine sediments (Jbel Rhassoul, Morocco). *Clays & Clay Minerals, 45*, 378–389.

Clark, R.N. (1999). Spectroscopy of rocks & minerals, & principles of spectroscopy. Pp. 3–58 in: *Manual of Remote Sensing, Volume 3, Remote Sensing for the Earth Sciences* (A.N. Rencz, editor). John Wiley & Sons, New York.

Cuevas, J., Vigil de la Villa, R., Ramirez, S., Petit, S., Meunier, A., & Leguey, S. (2003). Chemistry of Mg smectites in lacustrine sediments from the Vicalvaro sepiolite deposit, Madrid Neogene basin (Spain). *Clays & Clay Minerals, 51*, 457–472.

Darragi, F., & Tardy, Y. (1987). Authigenic trioctahedral smectites controlling pH, alkalinity, silica, & magnesium concentrations in alkaline lakes. *Chemical Geology, 63*, 59–72.

Degen, M., Sadki, M., Bron, E., Köng, U., & Nénert, G. (2014). The Highscore suite. *Powder Diffraction,* Supplement S2, *29* S13–S18.

Dejoux, C. (1993). Benthic invertebrates of some saline lakes of the Sud Lipez region, Bolivia. *Hydrobiologia, 267*, 257–267.

DeMaster, D.J. (2003). The diagenesis of biogenic silica: chemical transformations occurring in the water column, seabed, & crust. Pp. 87–96 in: *Treatise on Geochemistry, Volume 7.04, Sediments, Diagenesis, & Sedimentary Rocks* (H.D Holl& & K.K Turekian editor). Elsevier.

Deocampo, D. M. (2005). Evaporative evolution of surface waters & the role of aqueous CO_2 in magnesium silicate precipitation: Lake Eyasi & Ngorongoro Crater, northern Tanzania. *South African Journal of Geology, 108*, 493–504.

Deocampo, D. (2015). Authigenic clay minerals in lacustrine mudstones. Pp. 49–64 in: *Paying Attention to Mudrocks: Priceless!: Geological Society of America Special Paper 515* (D. Larson, S.O. Egenhoff, & N.S. Fishman, editors). Geological Society of America.

Deocampo, D. M., Cuadros, J., Wing-Dudek, T., Olives, J., & Amouric, M. (2009). Saline lake diagenesis as revealed by coupled mineralogy & geochemistry of multiple ultrafine clay phases: Pliocene Olduvai Gorge, Tanzania. *American Journal of Science, 309*, 834–868.

Deocampo, D. M., Behrensmeyer, A. K., & Potts, R. (2010). Ultrafine clay minerals of the Pleistocene Olorgesailie Formation, southern Kenya rift: diagenesis & paleoenvironments of early hominins. *Clays & Clay Minerals, 58*, 294–310.

Ece, Ö. I., & Çoban, F. (1994). Geology, occurrence, & genesis of Eskişehir sepiolite, Turkey. *Clays & Clay Minerals, 42*, 81–92.

Elzea, J. M., Odom, I. E., & Miles, W. J. (1994). Distinguishing well ordered opal-CT & opal C from high temperature cristobalite by X-ray diffraction. *Analytica Chimica Acta, 286*, 107–116.

Farr&, W. H., Glotch, T. D., Rice, J. W., Hurowitz, J. A., & Swayze, G. A. (2009). Discovery of jarosite within the Mawrth Vallis region of Mars: implications for the geological history of the region. *Icarus, 204*, 478–488.

Flower, R. J., & Ryves, D. B. (2009). Diatom preservation: differential preservation of sedimentary diatoms in two saline lakes. *Acta Botanica Croatica, 68*, 381–399.

Furquim, S. A. C., Barbiéro, L., Graham, R. C., Neto, J. P. Q., Ferreira, R. P. D., & Furian, S. (2010). Neoformation of micas in soils surrounding an alkaline-saline lake of Pantanal Wetl&, Brazil. *Geoderma, 158*, 331–342.

Gac, J. Y., Droubi, A., Fritz, B., & Tardy, Y. (1977). Geochemical behaviour of silica & magnesium during the evaporation of waters in Chad. *Chemical Geology, 19*, 215–228.

Galán, E. & Castillo, A. (1984). Sepiolite-palygorskite in Spanish tertiary basins: Genetical patterns in continental environments. Pp. 87–124 in: *Palygorskite-Sepiolite Occurrences, Genesis, & Uses* (A. Singer & E. Galán, editors). Developments in Sedimentology, *37*, Elsevier, Amsterdam, The Netherl&s.

Galán, E. & Pozo, M. (2011). Palygorskite & sepiolite deposits in continental environments. Description, genetic patterns, & sedimentary settings. Pp. 125–173 in: *Developments in Clay Science, Vol. 3, Developments in Palygorskite-Sepiolite Research, A New Outlook on these Nanomaterials* (E. Galán, & A. Singer, editors). Elsevier, Amsterdam, the Netherl&s.

García-Romero, E., Suárez, M., Santaré, J., & Alvarez, A. (2007). Crystallochemical characterization of the palygorskite & sepiolite from the Allou Kagne deposit, Senegal. *Clays & Clay Minerals, 55*, 606–617.

Gürel, A., & Özcan, S. (2016). Paleosol & dolocrete associated clay mineral occurrences in siliciclastic red sediments of the Late Miocene Kömişini Formation of the Tuzgölü basin in central Turkey. *Catena, 143*, 102–113.

Hardie, L. A., & Eugster, H. P. (1970). The evolution of closed-basin brines. *Mineralogical Society of America Special Paper, 3*, 273–290.

Hay, R. L. (1970). Silicate reactions in three lithofacies of a semi-arid basin, Olduvai George, Tanzania. *Mineralogical Society of America Special Paper, 3*, 237–255.

Hay, R. L., & Kyser, T. K. (2001). Chemical sedimentology & paleoenvironmental history of Lake Olduvai, a Pliocene lake in northern Tanzania. *Bulletin of the Geological Society of America, 113*, 1505–1521.

Hay, R. L., Guldman, S. G., Matthews, J. C., L&er, R. H., Duffin, M. E., & Kyser, T. K. (1991). Clay mineral diagenesis in Core Km-3 of Searles Lake, California. *Clays & Clay Minerals, 39*, 84–96.

Hecky, R. E., & Kilham, P. (1973). Diatoms in alkaline saline lakes: ecology & geochemical implications. *Limnology & Oceanography, 18*, 53–71.

Hover, V. C., & Ashley, G. M. (2003). Geochemical signatures of paleodepositional & diagenetic environments: a STEM/AEM study of authigenic clay minerals from an arid rift basin, Olduvai Gorge, Tanzania. *Clays & Clay Minerals, 51*, 231–251.

Hover, V. C., Walter, L. M., Peacor, D. R., & Martini, A. M. (1999). Mg-smectite authigenesis in a marine evaporative environment, Saline Ometepec, Baja, California. *Clays & Clay Minerals, 47*, 252–268.

Huggett, J., Cuadros, J., Gale, A., Wray, D., & Adetunji, J. (2016). Low temperature, authigenic illite & carbonates in a mixed dolomite-clastic lagoonal & pedogenic setting, Spanish Central System, Spain. *Applied Clay Science, 132–133*, 296–312.

Jones, B.F. (1986). Clay mineral diagenesis in lacustrine sediments. Pp. 291–300 in: *Studies in Diagenesis* (F.A. Mumpton, editor). *Bulletin of the US Geological Survey,* 1578.

Jones, B.F. & Galán, E. (1988). Sepiolite & palygorskite. Pp. 631–674 in: *Hydrous Phyllosilicates (Exclusive of Micas)* (S.W. Bailey, editor). Reviews in Mineralogy, *19*, Mineralogical Society of America, Washington, D.C.

Jones, B. F., & Weir, A. H. (1983). Clay mineral of Lake Abert, an alkaline, saline lake. *Clays & Clay Minerals, 31*, 161–172.

Kadir, S., Eren, M., & Atabey, E. (2010). Dolocretes & associated palygorskite occurrences in siliciclastic red mudstones of the Sariyer Formation (Middle Miocene), southeastern side of the Çanakkale Strait, Turkey. *Clays & Clay Minerals, 58*, 205–219.

Kadir, S., Erkoyun, H., Erin, M., Hugettt, J., & Önalgil, N. (2016). Palygorskite in Neogene lacustrine sediments, Eskişehir Province, West Central Anatolia, Turkey. *Clays & Clay Minerals, 64*, 145–166.

Kalro, Y. P. (1995). Determination of pH of soils by different methods: collaborative study. *Journal of AOAC International, 78*, 310–324.

Larsen, D. (2008). Revisiting silicate authigenesis in the Pliocence-Pleistocene Lake Tecopa beds, southeastern California: Depositional & hydrological controls. *Geosphere, 4*, 612–639.

Léveillé, R. J., Longstaffe, F. J., & Fyfe, W. S. (2002). Kerolite in carbonate-rich speleothems & microbial deposits from basaltic caves, Kauai, Hawaii. *Clays & Clay Minerals, 50*, 517–527.

Loucaides, S., Van Cappellen, P., Roubeix, V., Moriceau, B., & Ragueneau, O. (2012). Controls on the recycling & preservation of biogenic silica from biomineralization to burial. *Silicon, 4*, 7–22.

Martin De Vidales, J. L., Pozo, M., Alia, J. M., Garcia-Navarro, F., & Rull, F. (1991). Kerolite-stevensite in mixed layers from the Madrid Basin, central Spain. *Clay Minerals, 26*, 329–342.

Meunier, A. (2005). *Clays.* Springer, Berlin, 472 pp.

Michalopouos, P., Aller, R. C., & Reeder, R. J. (2000). Conversion of diatoms to clays during early diagenesis in tropical, continental shelf muds. *Geology, 28*, 1095–1098.

Milliken, R. E., Swayze, G. A., Arvidson, R. E., Bishop, J. L., Clark, R. N., Ehlmann, B. L., Green, R. O., Grotzinger, J. P., Morris, R. V., Murchie, S. L., Mustard, J. F., & Weitz, C. (2008). Opaline silica in young deposits on Mars. *Geology, 36*, 847–850. https://doi.org/10.1130/G24967A.1.

Milliken, R.E., Grotzinger, J.P., & Thomson, B.J. (2010). Paleoclimate of Mars as captured by the stratigraphic record in Gale Crater. *Geophysical Research Letters 37*, https://doi.org/10.1029/2009GL041870.f.

Moore, D. M., & Reynolds, R. C. (1989). *X-Ray Diffraction & the Identification & Analysis of Clay Minerals* (pp. 179–201). New York: Oxford University Press.

Papke, K. G. (1972). A sepiolite-rich playa deposit in southern Nevada. *Clays & Clay Minerals, 20*, 211–215.

Pozo, M., & Casas, J. (1999). Origin of kerolite & associated Mg clays in palustrine-lacustrine environments. The Esquivias deposit (Neogene Madrid basin, Spain). *Clay Minerals, 34*, 395–418.

Pozo, M. & Calvo, J.P. (2018). An overview of authigenic magnesian clays. *Minerals, 8*, https://doi.org/10.3390/min8110520.

Risacher, F., & Fritz, B. (1991). Geochemistry of Bolivian salars, Lipez, southern Altiplano: Origin of solutes & brine evolution. *Geochimica et Cosmochimica Acta, 55*, 687–705.

Ryves, D. B., Battarbee, R. W., Juggins, S., Fritz, S. C., & &erson, N. J. (2006). Physical & chemical predictors of diatom dissolution in freshwater & saline lake sediments in North America & West Greenl&. *Limnology & Oceanography, 51*, 1355–1368.

Santiago de Buey, C., Barrios, M. S., Romero, E. G., & Montoya, M. D. (2000). Mg-rich smectite "precursor" phase in the Tagus basin, Spain. *Clays & Clay Minerals, 48*, 366–373.

Servant-Vildary, S., & Roux, M. (1990). Multivariate analysis of diatoms & water chemistry in Bolivian saline lakes. *Hydrobiologia, 197*, 267–290.

Stoessell, R. K., & Hay, R. L. (1978). The geochemical origin of sepiolite & kerolite at Amboseli, Kenya. *Contributions to Mineralogy & Petrology, 65*, 255–267.

Story, S., Bowen, B.B., Benison, K.C. & Schulze, D.G. (2010). Authigenic phyllosilicates in modern acid saline lake sediments & implications for Mars. *Journal of Geophysical Research*, *115*, https://doi.org/10.1029/2010JE003687

Sylvestre, F., Servant-Vildary, S., & Roux, M. (2001). Diatom-based ionic concentration & salinity models from the south Bolivian Altiplano (15–23°S). *Journal of Paleolimnology, 25*, 279–295.

Tosca N.J. (2015). Geochemical pathways to Mg-silicate formation. Pp. 283–330 in: *Magnesian Clays: Characterization, Origin, & Applications* (M. Pozo & E. Galan, editors). Bari, Italy.

Tosca, N. J., & Masterson, A. L. (2014). Chemical controls on incipient Mg-silicate crystallization at 25°C: Implications for early & late diagenesis. *Clay Minerals, 49*, 165–194.

Tosca, N. J., Macdonald, F. A., Strauss, J. V., Johnston, D. T., & Knoll, A. H. (2011). Sedimentary talc in Neoproterozoic carbonate successions. *Earth & Planetary Science Letters, 306*, 11–22.

Turner, C. E., & Fishman, N. S. (1991). Jurassic Lake T'oo'dichi': A large alkaline, saline, lake, Morrison Formation, eastern Colorado Plateau. *Bulletin of the Geological Society of America, 103*, 538–558.

Tutulo, B. M., & Tosca, N. J. (2018). Experimental examination of the Mg-silicate-carbonate system at ambient temperature: Implications for alkaline chemical sedimentation & lacustrine carbonate formation. *Geochimica et Cosmochimica Acta, 225*, 80–101.

Weaver, C.E. (1989). *Clays, Muds, & Shales.* 820 pp. Elsevier, Amsterdam.

Wray, J. J., Squyres, S. W., Roach, L. H., Bishop, J. L., Mustard, J. F., & Dobrea, E. Z. N. (2010). Identification of the Ca-sulfate bassanite in Mawrth Vallis, Mars. *Icarus, 209*, 416–421.

Wray, J.J., Milliken, R.E., Dundas, C.M., Swayze, G.A., &rews-Hanna, J.C., Baldridge, A.M., Chojnacki, M., Bishop, J.L., Ehlmann, B.L., Murchie, S.L., Clark, R.N., Seelos, F.P., Tornabene, L.L., & Squyres, S.W. (2011). Columbus crater & other possible groundwater-fed paleolakes of Terra Sirenum, Mars. *Journal of Geophysical Research*, *116*, https://doi.org/10.1029/2010JE003694

(Received 14 December 2018; revised 15 February 2020; AE: Warren D. Huff)